MASTER'S DISSERTATION

Breaking the limits of low surface brightness in Ultraviolet

Ignacio Ruiz Cejudo

Academic course: 2023-24
Supervisor: Ignacio Trujillo Cabrera

July, 2nd 2024

Abstract

In recent years, various optical surveys have reached unprecedented depths ($\gtrsim 30\,\mathrm{mag\,arcsec^{-2}}$), facilitating the study of fainter galactic structures. However, ultraviolet bands, which are key for the study of the stellar populations, remain basically unexplored at these depths. In this work, we present a low surface brightness analysis of several nearby galaxies observed by GALEX in the FUV and NUV, adapting and applying methods proven effective in optical surveys.

We use data from different GALEX programs of 17 galaxies (13 in FUV). 16 of these galaxies are observed by LIGHTS survey, with IC3211 being in one of the fields. A novel approach to background subtraction is proposed, whereby the deviation of the UV background from a Gaussian distribution is modelled as a Poisson process. Furthermore, the PSF deconvolution algorithms developed for optical data are applied in our sample, using a novel set of PSFs for the GALEX bands.

This methodology enables the acquisition of reliable surface brightness profiles with depths of $\sim\ 28.5 - 31\,\mathrm{mag\,arcsec^{-2}}$ $(3\sigma; 10'' \times 10'')$, around 1 mag deeper than with the standard techniques. Furthermore, we demonstrate that the application of PSF deconvolution, particularly in FUV, effectively mitigates the excess of light present in the outer regions of certain galaxies when compared to the standard GALEX pipeline. A qualitative analysis of the results is presented, with a particular focus on the study of stellar populations at the edge of galaxies. Low surface brightness friendly algorithms in the UV, applied to the study of edges, will allow us to explore the mechanisms of in-side out growth of the galaxies with much more accuracy.

Keywords: methods: data analysis - galaxies: evolution - galaxies: stellar content - galaxies: photometry - ultraviolet: galaxies

Resumen

El estudio de la formación y evolución de las galaxias desde el punto de vista observacional ha experimentado un avance significativo en los últimos años. El desarrollo de telescopios más potentes y de nuevas técnicas de observación y análisis de las imágenes está permitiendo estudiar regiones y propiedades de las galaxias hasta ahora inexploradas. Uno de los avances más significativos consiste en el estudio del bajo brillo superficial ($\mu_V \gtrsim 27\,\mathrm{mag\,arcsec^{-2}}$). Gracias al uso de telescopios de más de 8 metros (como GTC, LBT o Subaru, entre otros), junto con el desarrollo de nuevas técnicas de observación y análisis de datos, se están consiguiendo imágenes de gran profundidad en bandas ópticas, llegando a brillos de hasta $\mu_V \sim 31\,\mathrm{mag\,arcsec^{-2}}$ ($3\sigma; 10'' \times 10''$; Trujillo & Fliri 2016). Estas profundidades han abierto la puerta al estudio de estructuras hasta ahora ocultas, como es el caso de los halos estelares o los bordes de las galaxias más allá del Grupo Local. Su estudio puede ayudar a entender los procesos de formación y evolución de dichas galaxias. Recientemente, se han desarrollado varios cartografiados con el objetivo de alcanzar dichas profundidades, tales como el futuro *Large Synoptic Survey Telescope* (Ivezić et al. 2019), o el reciente *LBT Imaging of Galaxy Haloes and Tidal Structures Survey* (LIGHTS, Trujillo et al. 2021).

Sin embargo, para poder realizar un estudio completo de estas regiones, es necesario contar con datos en otras longitudes de onda como el Ultravioleta, región del espectro con información vital sobre las formaciones estelares más recientes. Con telescopios espaciales como GALEX, diferentes trabajos han proporcionado estudios de las poblaciones estelares a profundidades relativamente altas, logrando identificar estructuras de bajo brillo superficial tales como los *discos extendidos en UV* (X-UV disks, Thilker et al. 2007). Sin embargo, las técnicas más recientes asociadas al estudio de bajo brillo superficial aún no han sido aplicadas a estos datos. En este trabajo, hemos aplicado estas técnicas al estudio de galaxias en el Ultravioleta con datos de GALEX en las bandas del UV cercano (NUV) y lejano (FUV). Para ello, hemos seleccionado 16 galaxias de la muestra de LIGHTS (12 en FUV) con tiempos de exposición superiores a 1000 s, añadiendo una galaxia en uno de los campos de LIGHTS (IC3211).

Este estudio se fundamenta en el desarrollo de una nueva metodología para el análisis de datos de GALEX basada en trabajos previos tanto en el óptico como en el UV. Esta metodología consta de dos partes fundamentales: la caracterización del brillo de fondo y detección de fuentes; y la caracterización y sustracción del efecto de la PSF. Primero, realizamos una detección de fuentes en el NUV, y utilizamos esta para enmascarar ambas bandas y caracterizar el brillo de fondo con su media. Una vez caracterizado, lo sustraemos de la imagen construyendo la distribución de Poisson asociada a esta media. El objetivo de este tipo de sustracción es no solo conseguir un brillo de fondo nulo, si no también transformar la naturaleza Poissoniana del brillo de fondo en el UV (ver por ejemplo, Gil de Paz et al. 2007) en una distribución casi Gaussiana, para poder aplicar algoritmos de detección tales como NoiseChisel (Akhlaghi 2019a), optimizados para estructuras de bajo brillo superficial.

Posteriormente, caracterizamos el efecto de las PSF en cada galaxia aplicando la metodología desarrollada para la parte óptica de LIGHTS por Golini et al. (in prep.). Esta está basada en los algoritmos de deconvolución de Wiener (Hunt 1971) y la descomposición fotométrica de la galaxia, asumiendo que el principal efecto de la PSF se ve en su convolución con el modelo de la galaxia. Para ello, hemos construido nuevas PSFs para las bandas de GALEX, extendiendo las disponibles en los archivos hasta $750''$, pero usando datos reales de estrellas. Esto es debido a que las colas de las PSFs originales parecen infraestimar las colas de las estrellas más brillantes, haciendo que disminuya el efecto de la convolución del modelo con las mismas.

Gracias a la aplicación de esta metodología, conseguimos imágenes con un brillo superficial límite ($3\sigma; 10'' \times 10''$) de entre 28.5 y 30.5 $\mathrm{mag\,arcsec^{-2}}$, con perfiles alcanzando valores creíbles de hasta $31\,\mathrm{mag\,arcsec^{-2}}$. Estos valores suponen hasta 1 magnitud más profundos que otros trabajos usando datos de GALEX (Bouquin et al. 2018 entre otros), permitiendo detectar el borde de las galaxias (definido por Trujillo et al. 2020) en el 76 % de la muestra.

Para analizar la validez de nuestra metodología, hemos comparado nuestros resultados con la pipeline de GALEX (Morrissey et al. 2007). Gracias a esta comparación, vemos que nuestra forma de medir y sustraer el brillo de fondo evita sobre-sustracciones debidas a estructuras en el brillo de fondo presentes

en la pipeline de GALEX, en algunos casos asociadas a una pobre detección de fuentes. El resultado más notable de nuestra metodología, sin embargo, está relacionado con el efecto de la PSF. Somos capaces de demostrar que, en algunas galaxias de la muestra, no tomar en cuenta el efecto de la convolución con la PSF en la banda FUV lleva a un exceso de brillo en las partes más externas de las galaxias, haciendo también que los colores FUV-NUV sean extremadamente azules en estas regiones. Dado que la luminosidad en FUV y el color FUV-NUV están estrechamente relacionados con la formación estelar y la edad de las poblaciones estelares (Bianchi 2011), la sustracción de este efecto es crucial en el estudio de las poblaciones estelares en las afueras de las galaxias.

Finalmente, aprovechamos las profundidades de nuestros resultados para dar una interpretación cualitativa de los perfiles de brillo y color. Primero, analizamos la validez de los bordes detectados en los perfiles, prestando especial atención a aquellos casos donde la definición de un solo borde parece difícil y a qué es debido esto. Por otro lado, tratamos de localizar algunas estructuras de bajo brillo superficial, centrándonos en un posible disco extendido y preguntándonos si es posible detectar halos estelares en el NUV. El trabajo concluye con un primer estudio cuantitativo de los ratios de formación estelar y edades de dos galaxias, analizando la validez de los resultados y los límites de las calibraciones utilizadas.

En resumen, este trabajo presenta una metodología novedosa para el estudio de la parte Ultravioleta de las galaxias. Con unos algoritmos centrados en el bajo brillo superficial, esperamos que, aplicados al estudio de los bordes de las galaxias, esta metodología nos permita explorar los mecanismos de crecimiento de las galaxias con mucho más detalle.

Palabras clave: métodos: análisis de datos - galaxias: evolución - galaxias: contenido estelar - galaxias: fotometría - ultravioleta: galaxias

Contents

Chapter 1

Introduction and objectives

The study of the formation and evolution of galaxies has undergone a significant evolution in recent years, due to the development of new and more advanced technology and techniques. At high redshift, the recent launch of the *James Webb Space Telescope* is facilitating the exploration of young galaxies with resolutions never previously achieved, challenging our comprehension of the early stages of galactic evolution. At low redshift, one of the most significant advances has been the acquisition of increasingly deeper data. In this context, works like Jablonka et al. (2010) or Trujillo & Fliri (2016) demonstrate that, with an optimal observation and analysis strategy, it is possible to reach depths of $\mu_V \gtrsim 30\,\mathrm{mag\,arcsec^{-2}}$ (3σ; $10'' \times 10''$). Such depths have recently been reached by wide surveys such as the Hyper Suprime Cam Survey (Aihara et al. 2018), and are expected for the Large Synoptic Survey Telescope (LSST; Ivezić et al. 2019).

These depths are enabling the study of galactic structures that were previously inaccessible beyond the Local Group with resolved stellar population studies. In a cosmological model based on the ΛCDM, works like Cooper et al. (2010) showed that almost all present-day galaxies will exhibit a stellar halo. However, the depths required to observe this phenomenon must exceed $\mu_V \sim 31\,\mathrm{mag\,arcsec^{-2}}$ (Bullock & Johnston 2005). In a recent study, Martínez-Delgado et al. (2023) used data from DESI to demonstrate the previously undetected tidal structures associated with the dwarf satellite interactions in nearby galaxies, which are present in the stellar halos of host galaxies. Other stellar streams have been identified at comparable depths (e.g., Román et al. 2023). In this context, the LBT Imaging of Galaxy Haloes and Tidal Structures (LIGHTS) survey (Trujillo et al. 2021; Zaritsky et al. 2024) aims to identify systematically these haloes and streams through 1 to 2 mag $\mathrm{arcsec^{-2}}$ deeper observations of a sample of nearby galaxies with the LBT.

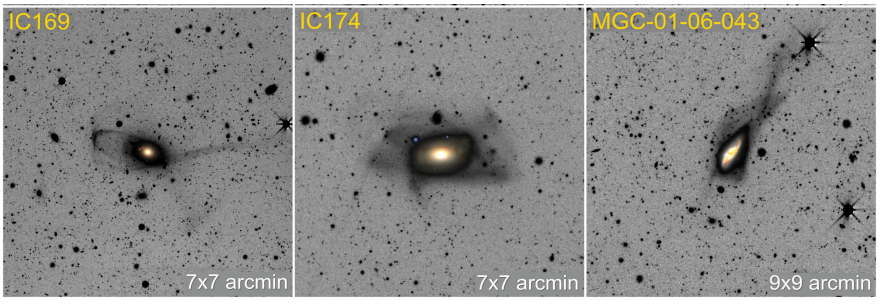

Figure 1.1: Examples of stellar streams from Martínez-Delgado et al. (2023) (Fig. 3, 2nd row of their work).

These depths have also permitted the investigation of the borders of galaxies. In Trujillo et al. (2020) and Chamba et al. (2022) a novel definition for the size of the galaxy was proposed. This definition is based on a physical motivation: beyond a certain radius, the surface stellar density is below the threshold for in-situ star formation ($\Sigma_* \sim 1\,\mathrm{M_\odot pc^{-2}}$ for local spirals, Trujillo et al. 2020). This radius, R_{edge}, can be located by the surface brightness profiles, since it is connected with the truncation observed in the profile.

Furthermore, this definition is both physically motivated and empirically validated, exhibiting a 2.5-times reduction in intrinsic scatter compared to the effective radius (Trujillo et al. 2020) and demonstrating a pronounced size evolution since redshift z=1 (Buitrago & Trujillo 2024).

Given that this R_{edge} is linked to the process of star formation within the galaxy, an investigation into the stellar populations present in the vicinity of the galaxy's edges could provide insights into the formation and evolution of these edges. In this context, an ultraviolet analysis of these regions may help in these studies. The UV region of spectra is mainly connected to the youngest stars (Bruzual & Charlot 2003) of galaxies, and is one of the most effective tracers of recent star formation activity in galaxies (up to 100 Myr; see, e.g., Kennicutt & Evans 2012). In 2003, NASA launched the mission *Galaxy Evolution Explorer* (GALEX, Martin et al. 2005), with the objective of studying the star formation history at low-intermediate redshifts. GALEX covers both far-UV and near-UV bands in a wide field of view ($\sim 1°.25$), providing UV imaging that is highly sensitive to star formation, even at low levels. Its colour profiles also serve as a proxy for the stellar population ages (Bianchi 2011). It is therefore unsurprising that GALEX data has been used to investigate the stellar populations of galaxies, even in low surface brightness regimes. One example of this is the discovery of so-called Extended Ultraviolet Disks (XUV-disks) by Gil de Paz et al. (2005) and Thilker et al. (2005). These are star forming regions at galactocentric distances further than expected from the optical images of that era. Thilker et al. (2007) reported that at least 20% of present-day spiral galaxies may possess XUV-disks, suggesting that the formation of these outer disks may be a key aspect of galaxy evolution.

It can be reasonably assumed that the techniques applied recently in low surface brightness astronomy in the optical have not been tested with GALEX data, unless some studies in low surface brightness using GALEX had been carried out (e.g., Boissier et al. 2008). Moreover, it is not possible to apply all the techniques developed for such studies, since one of the main advances in low surface brightness is the development of a proper observation strategy (see, e.g., Trujillo & Fliri 2016). Despite these limitations, some techniques remain applicable to the analysis of GALEX data. One of the principal steps in the analysis of low surface brightness studies is the process of background subtraction. In their study, Kelvin et al. (2023) used simulated data based on the HSC-SSP to assess the accuracy of different background measurements produced by various source detection programs. Their findings highlight the crucial role of accurate background measurements in the detection of faint objects. In addition, Watkins et al. (2024) conducted a comprehensive analysis of various background subtraction techniques and their efficacy in low surface brightness studies.

Another factor to be considered when analyzing low surface brightness features of galaxies is the Point Spread Function (PSF). As evidenced by works like De Jong (2008) or Sandin (2014), the PSF effect results in brighter profiles at the outskirts of galaxies. Consequently, failure to consider the impact of the PSF may result in erroneous interpretations of the outermost regions of surface brightness profiles. In this context, Golini et al. (in prep.) is developing a new technique to subtract these effects for LIGHTS data.

In this study, we aim to perform a low surface brightness analysis of GALEX data, with the objective of providing the ultraviolet counterpart of the galaxies in the ultra-deep LIGHTS optical survey and useful data for studying the stellar populations at the outskirts of these galaxies (an example of the difference between LIGHTS optical data and GALEX UV data is presented in the colour composed images of NGC1042, Fig. 1.2). In order to achieve this, we present a new methodology for the analysis of the data, based on the strategies developed for the optical imaging. The work is divided as follows:

1. In Sec. 2, we present the sample selection, with a total of 16 LIGHTS galaxies (12 in FUV) and an additional galaxy in one of the fields of view.

2. In Sec. 3, we present the methodology applied in our work. This methodology is based on two main steps: the background subtraction and the PSF deconvolution.

3. In Sec. 4, we show the results of applying the aforementioned methodology. These results are presented in the form of surface brightness and colour profiles, in addition to the measured limits.

4. In Sec. 5.1, we compare our results with those obtained by the standard GALEX pipeline. This comparison allows us to discern whether our methodology improves upon the results of previous work.

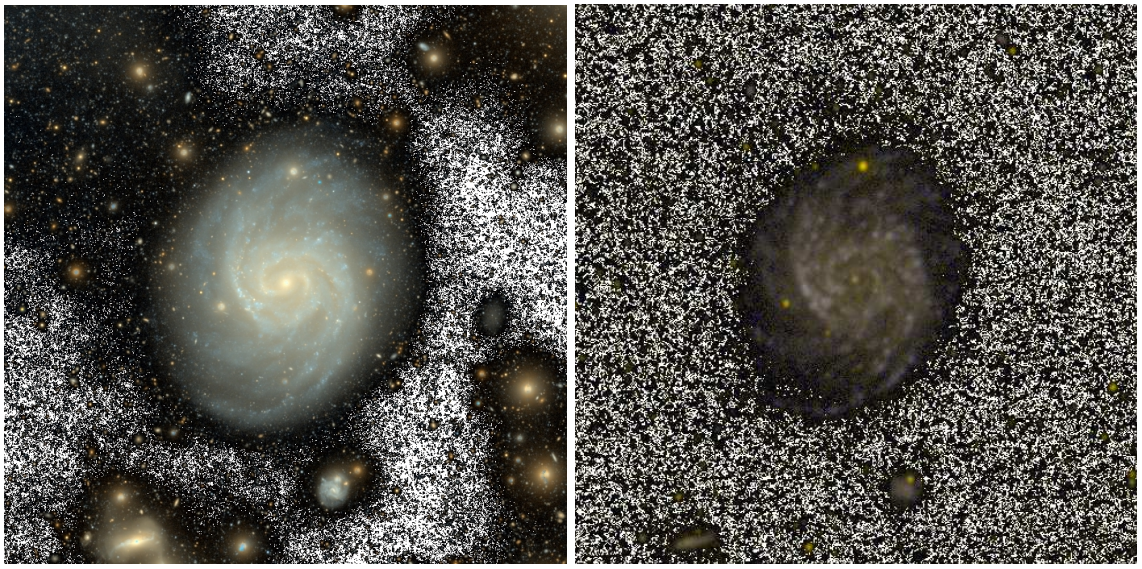

Figure 1.2: Colour images of NGC1042 ($13' \times 13'$). Left: crop of LIGHTS LBT colour composed image (see Trujillo et al. 2021, Fig. 2). Right: UV composed image with the data reduced with the methodology described in Sec. 3. The strategy for compose this colour image is similar to the one of Gil de Paz et al. (2007), but using GNUAstro's tool color-faint-gray (Infante-Sainz & Akhlaghi 2024).

Then, in Sec. 5.2, we present a qualitative analysis of the resulting profiles, including preliminary measurements of stellar ages and star formation rates.

5. We summarize the main conclusions of our work in Sec. 6

In all the work, magnitudes are in the AB system (Oke & Gunn 1983).

Chapter 2

Sample Selection

The selection of galaxies studied in this work is based on the LIGHTS survey (Trujillo et al. 2021; Zaritsky et al. 2024). The survey comprises a total of 25 nearby galaxies (to date), selected according to the criteria outlined in Zaritsky et al. (2024). The selection criteria were primarily determined by instrumental limitations (such as the Field-of-view, FOV, of the LBT camera), and by the scientific aims of the survey (including the ability to distinguish between extended stellar disk and halo components and the detection of low surface brightness satellite galaxies). The galaxies in the sample are, in general, nearby spiral galaxies that exhibit morphological characteristics and stellar mass similar to those of the Milky Way or a bit lower. These galaxies are particularly relevant because they have been studied in depth in cosmological simulations, and we therefore have extensive predictions of how they should grow. Notable exceptions in the LIGHTS survey are NGC4220 and NGC5866, which have been classified as S0-a (Zaritsky et al. 2024, Fig. 1).

UV data for these galaxies was obtained from the *Galaxy Evolution Explorer* (GALEX, Martin et al. 2005) satellite GR6 and GR7 data releases (Bianchi et al. 2014). GALEX was a NASA Explorer Mission, launched on April 2003, which conducted a space-based sky survey in the UV bands near-UV (NUV, 1771-2831 Å, $m_{\rm ZP} = 20.08$) and far-UV (FUV, 1344-1786 Å, $m_{\rm ZP} = 18.82$). Both bands were surveyed with a plate scale of $1.5''/pixel$. The field of view is $1°.24/1°.28$, with a spatial resolution of $5''.3/4''.2$ for NUV/FUV respectively (Morrissey et al. 2007). A summary of the surveys conducted and the scientific highlights achieved can be found in Bianchi (2014).

The data were retrieved from three distinct surveys: the *Nearby Galaxy Survey* (NGS, Gil de Paz et al. 2007), the *Medium Imaging Survey* (MIS), the *Deep Imaging Survey* (Deep-DIS, Bianchi et al. 2017; Morrissey et al. 2007), in addition to public data from guest investigator programs (GII). All data is publicly available in the MAST archives[1]. In order to ensure sufficient depth of data for the analysis, $\mu_{lim} \gtrsim 28.5\,\mathrm{mag\,arcsec^{-2}}$ (3σ; $10'' \times 10''$), only images with exposures exceeding 1000s are selected. This selection criterion results in the identification of 16 galaxies (12 in FUV), which are summarized in Table 2.1. Additionally, IC3211, a spiral galaxy in the field of NGC4307, is included in the analysis, serving to test the methodology in a smaller (in apparent size) galaxy. In all cases, we utilise count maps (*-cnt*) and high-resolution relative response maps (*-rrhr*). In order to comply with the methodology, we transform the counts into intensity by $int = \frac{cnt}{rrhr}$ rather than downloading the intensity maps. Furthermore, background-subtracted intensity maps (*-intbgsub*) are employed for comparison with the methodology presented in this work.

[1] https://galex.stsci.edu/GR6/

Table 2.1: List of galaxies analyzed in this work. The geometry (position angle and ellipticity) is based on the LBT g-band observations (Zaritsky et al. 2024). Coordinates and distances are taken from the same work, with the exception of IC3211, whose data is taken from Ahn et al. (2012).

Name	RA [deg]	DEC [deg]	D [Mpc]	PA (1)	b/a	Survey	$t_{\rm exp}$ [s]		$F_{\rm bck}$ (2) [counts]		$\mu_{lim}(3\sigma, 10'' \times 10'')$ [mag arcsec^2]	
							NUV	FUV	NUV	FUV	NUV	FUV
NGC1042	40.09986	-8.43354	13.5	75°	0.83	NGS	3775.7	2949.5	7.755	0.649	29.17	29.09
NGC2712	134.87698	44.91390	30.2	90°	0.54	MIS	1691.05	- (3)	2.991	-	28.77	-
NGC2903	143.04212	21.50083	10.0	110°	0.42	NGS	1909.2	1910.2	4.597	0.411	28.67	28.79
NGC3049	148.70652	9.27109	19.3	149°	0.64	NGS	3172.2	1482.1	7.152	0.427	28.95	28.56
NGC3198	154.97897	45.54962	12.9	126°	0.36	NGS	16587.95	14904.90	26.272	1.925	30.00	30.26
NGC3351	160.99042	11.70381	10.0	100°	0.72	NGS	1692.2	1692.2	4.028	0.351	28.58	28.81
NGC3368	161.69058	11.81994	11.2	80°	0.60	NGS	11450.75	4529.15	24.784	0.776	29.69	29.32
NGC3486	165.09945	28.97514	13.6	−10°	0.77	GII	4023.65	2439.65	6.925	0.430	29.18	29.06
NGC3596	168.77586	14.78702	11.3	149°	0.92	GII	1661.05	-	3.908	-	28.61	-
NGC3972	178.93787	55.32074	20.8	27°	0.27	GII	2803.1	-	5.045	-	29.02	-
NGC4220	184.04880	47.88326	20.3	50°	0.33	DEEP-DIS	12101.10	12101.10	19.455	2.313	29.89	29.82
NGC4307	185.52368	9.04363	20.0	−67°	0.24	GII	6337.45	6337.45	12.824	1.073	29.42	29.69
NGC4321	185.72846	15.82182	15.2	70°	0.77	GII	6466.1	4805.1	12.880	0.914	29.45	29.46
NGC5248	204.38343	8.88518	14.9	17°	0.67	MIS	1648.1	-	3.479	-	28.73	-
NGC5866	226.62291	55.76321	14.1	38°	0.43	NGS	1526.4	1526.4	2.831	0.452	28.65	28.69
NGC5907	228.97404	56.32877	16.5	64°	0.13	GII	15118.45	1543.6	23.737	0.328	29.97	28.70
IC3211	185.53048	8.99056	85.0	-54°	0.89	GII	6337.45	6337.45	12.824	1.073	29.42	29.69

(1): Position angle from West anti-clockwise.
(2): Mean value of the background, see Sec. 3.1.
(3): If -, no data matches the t_{exp} selection criteria.

Chapter 3

Methodology

3.1. Background subtraction and mask building

The sources of the images are identified by using GNUAstro[1]'s tools NoiseChisel and Segment (Akhlaghi & Ichikawa 2015; Akhlaghi 2019a). The detection process has been optimised for the identification of low surface brightness features. This is achieved by constructing a detection map in which the background is treated as a uniform Gaussian distribution. The difference between quantiles of the mean and median is then employed to detect sources in the images. This approximation is effective in Gaussian backgrounds, such as those observed by ground-based optical and near-infrared telescopes, where the atmosphere brightness is very high. However, as previously noted by different works (e.g., Gil de Paz et al. 2007), the UV background is notably low, resulting in highly Poissonian statistics, particularly in FUV. Consequently, the application of NoiseChisel for the detection of large extended sources in FUV is not accurate, and depending on the exposure times on NUV, it also face problems in detecting the faintest parts of galaxies.

In order to circumvent this issue and permit the utilisation of NoiseChisel for the identification of the faintest objects in both NUV and FUV, we have implemented the following strategy:

1. A preliminary mask is constructed using NoiseChisel and Segment on the NUV count map, as the NUV background is relatively high and nearly Gaussian, and the detection threshold performs well in these images. This mask is then applied to both NUV and FUV, on the assumption that there are no only FUV sources. Nevertheless, a visual inspection is conducted to identify any FUV sources of light that have not been masked in NUV.

2. Following the masking of all sources, the mean of the background in both FUV and NUV is characterised by measuring it at distances relatively far from the galaxy to avoid scattered light, while also being close enough to ensure that the measurements are representative of the local background of the galaxy. The surface brightness profile is then examined to ascertain whether it is asymptotically dominated by background (i.e., flat). If this is the case, an annular region is selected for the measurement of the mean (μ). Subsequently, a random 2D Poisson distribution with $\mu = F_{bck}$ (Tab. 2.1) is constructed, and the resulting image is subtracted from the counts map. The result is an image where the background is similar to a Gaussian distribution centred on 0 (see Fig. 3.1, 3.2). This is equivalent to subtracting the mean value from a Gaussian background (see Appendix B for a math description of the subtraction of two Poisson distributions). It should be noted here that the work is being carried out on the counts map, not taking into account the response of the CCD (*-rrhr* images). This is because the Poisson distribution is defined in integer numbers (counts), while intensity maps have float values (counts per second). Unless the *-rrhr* includes a flat field correction (see Morrissey et al. 2007, Sec. 3.3), during the course of this work it was tested that the flat correction does not affect background measures.

3. Finally, the background-subtracted count maps are transformed into intensity images. The masks for NUV and FUV are then rebuilt individually using NoiseChisel and Segment. The main NoiseChisel parameters used for this task are: -tilesize=5,5 -meanmedqdiff=0.02 -outliersigma=3

[1] https://www.gnu.org/software/gnuastro/

-qthresh=0.7 -minskyfrac=0.7 -dthresh=2 -snminarea=3 -detgrowquant=0.8 -snthresh=3 ; with small variations between each field. After that, the final results are visually inspected, with any apparent sources that are too faint to be detected manually masked if necessary.

In all fields, we work with cropped images of dimensions $25' \times 25'$ ($37.5' \times 37.5'$ in the cases of NGC3198 and NGC5907) in order to avoid lengthy NoiseChisel execution times. The utilisation of cropped images also permits the avoidance of potential structural anomalies associated with vignetting or scattered light from external sources within the field when constructing the masks.

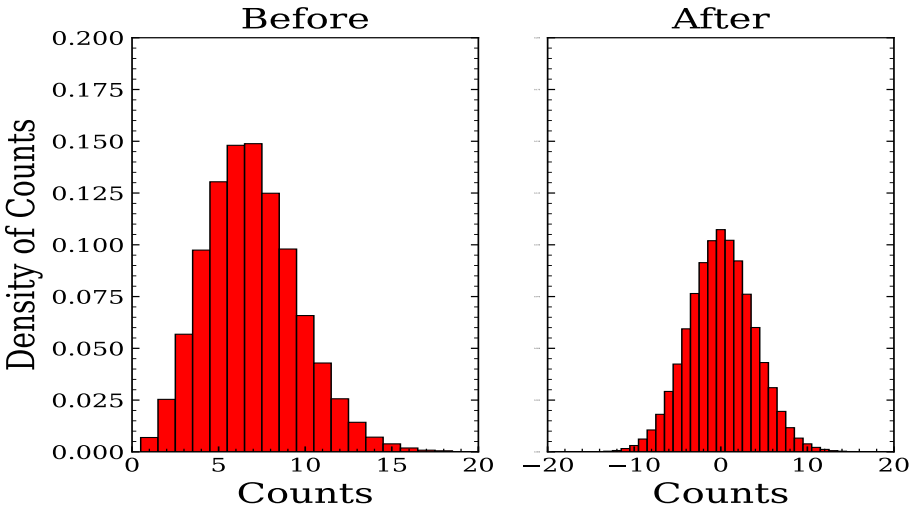

Figure 3.1: Histogram of background counts before and after statistical subtraction in NGC3486 NUV. The background is measured using pixels within an annular ellipse ring between $8.75'$ and $12.5'$ from the center of the object.

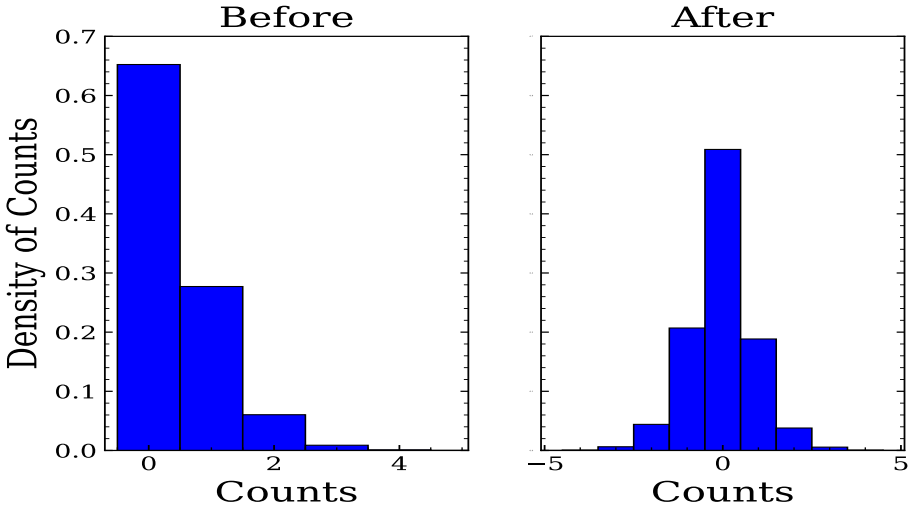

Figure 3.2: Same as Fig. 3.1 but on FUV.

3.2. PSF characterization and subtraction

The analysis of LIGHTS data has demonstrated that the PSF effects in the outskirts of galaxies play a major role in the surface brightness profiles and particularly in the colour profiles. In this study, we

have employed the methodology outlined in Golini et al. (in prep.) to analyse GALEX data. To this end, we have extended radically the GALEX PSFs up to $R = 750''$ by utilising PSF scripts of GNUAstro (Infante-Sainz et al. 2020), in order to obtain a comprehensive characterisation of the outermost regions of the galaxies. This radial extension is motivated by the typical extension of our objects ($D \sim 10$ arcmin), and following the prescription by Sandin (2014) of using PSF at least 1.5 times larger than the size (radius) of the objects.

The original GALEX PSFs were constructed in Morrissey et al. (2007) and are accessible at GALEX technical documentation[2]. These PSFs are characterised up to $R = 90''$ based on multiple observations of the star LDS749b (Morrissey et al. 2007, Sec. 5). A comparison between the Morrissey et al. (2007) PSFs and real stars from different fields and surveys indicates that extended PSFs based on the original ones underestimate the outer slopes of the real stars (Fig. 3.3).

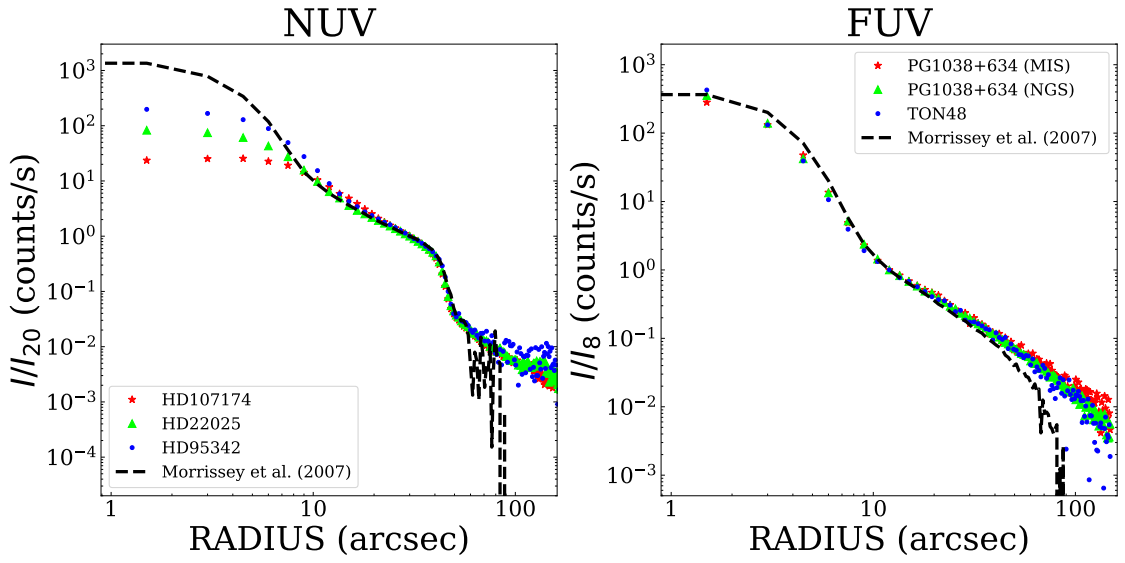

Figure 3.3: Profiles of different stars compared with GALEX PSFs (NUV left, FUV right). The stars are taken from different fields and surveys. In NUV: HD107174 is present at GII survey ($t_{exp} = 33700$s); HD22025 is at DEEP-DIS survey ($t_{exp} = 29000$s); and HD95342 is on NGC3486 field (see Tab. 2.1). In the cse of FUV: TON48 is present on NGC3486 field; while PG1038+634 is present in two different surveys: MIS ($t_{exp} = 1655$s) and NGS ($t_{exp} = 1568$s). The profiles are normalized to the value at $R = 20\,\mathrm{pix} = 30''$ for NUV (I_{20}) and at $R = 8\,\mathrm{pix} = 12''$ for FUV (I_8).

As a consequence of this underestimation, we have constructed new PSFs for GALEX bands based on different stars from various surveys. In all cases, the same masking and background subtraction methodology explained in Sec. 3.1 was employed. To avoid problems with saturation (see central regions of the profiles in Fig. 3.3), we have retained the core of the original GALEX PSFs by Morrissey et al. (2007), and characterise the outermost slopes. In the NUV, the original PSF has been retained up to a radius of $50''$, at which point the NUV PSF reverts to a Moffat profile. Utilising the stars presented in Fig. 3.3 (left), two distinct slopes where identified: $\beta_1 = -3.30$ between $50''$ and $75''$, and $\beta_2 = -2.01$ beyond $75''$. In the case of FUV, a single slope of $\beta = -2.15$ was determined, joined with the original PSF at $12''$. In both bands, the image was constructed with a radius of $750''$. The final PSFs are presented in Fig. 3.4 alongside the stars used for the construction.

[2] http://www.galex.caltech.edu/researcher/techdoc-ch5.html

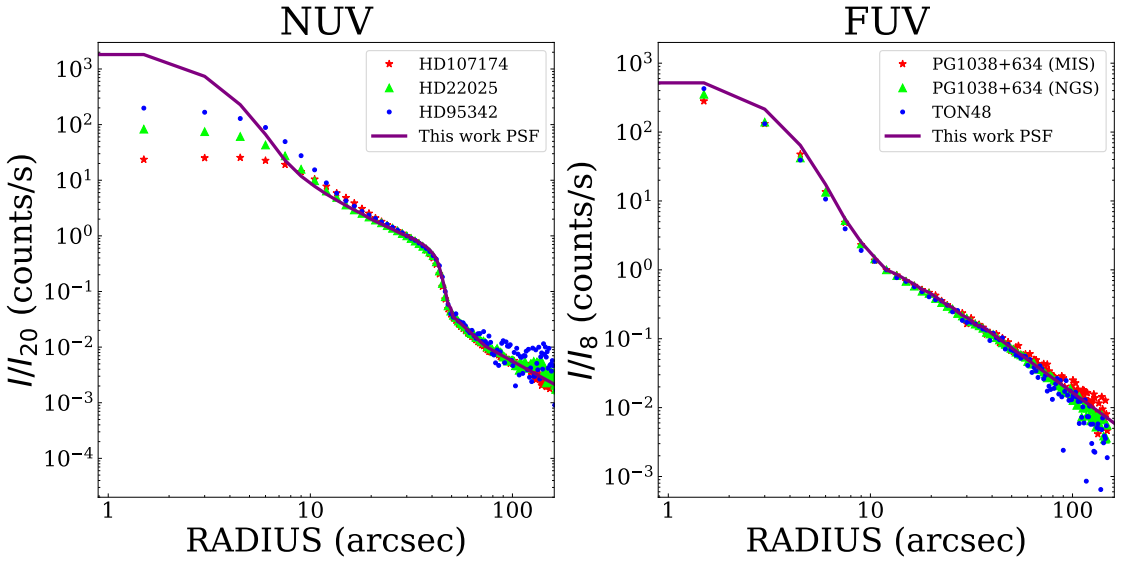

Figure 3.4: Same as Fig. 3.3, but with the PSFs built in this work.

Following the work of Golini et al. (in prep.), we have employed these novel PSFs to deconvolve the background-subtracted intensity maps through the application of the Wiener algorithm for deconvolution. The Wiener filter (Wiener 1949) is employed in this algorithm to recover a signal that has been affected by noise and degraded by an impulse response. If we consider that a certain image can be expressed as y:

$$y = Hx + n \tag{3.1}$$

where H is the impulse response (in our case the PSF), and n is the noise of the image; the Wiener deconvolution returns an estimation of the signal ($\hat{x}$) deconvolved from the impulse response. This estimation mitigates the effects of noise in a poor signal-to-noise ratio through the application of the Wiener filter in the frequency domain:

$$\hat{x} = F^{\dagger}\left(|\Lambda_H|^2 + \lambda|\Lambda_D|^2\right)^{-1}\Lambda_H^{\dagger}Fy \tag{3.2}$$

where $F, F^{\dagger}$ are the Fourier and inverse Fourier transforms, Λ_H represents the transfer function, and Λ_D is a filter to penalize restored image frequencies, with λ tuning the balance between data and regularization. The deconvolution was developed by Hunt (1971).

The algorithm is implemented in the Python package Scikit-Image, utilising the functions restoration.wiener and restoriation.unsupervised_wiener[3]. From these two, we have employed the unsupervised Wiener deconvolution, where the parameter λ is estimated automatically. Both functions were subjected to testing, with comparable outcomes.

It can be observed that, while this algorithm was introduced with the intention of mitigating the noise present in deconvolution processes, the result is noisier than the original. Consequently, Golini et al. (in prep.) utilise the deconvolved image not as the final image, but rather to characterise the photometric decomposition of the galaxy. Assuming that the PSF primarily affects the model of the galaxy (Eq. 3.3), with the effects on residuals playing a minor role on the profiles, they obtain an image deconvolved from the PSF by applying Eq. 3.4:

$$G_o = (M \otimes PSF) + R \tag{3.3}$$

$$G_d = M + R = M + [G_o - (M \otimes PSF)] \tag{3.4}$$

where G_o is the background subtracted image of the galaxy, G_d is the PSF deconvolved image of the galaxy, M is the model obtained from the Wiener deconvolved image, and R are the residuals of subtracting the

[3] Skimage.restoration manual

model convolved with PSF from G_o.

The aforementioned methodology is employed to characterise the models in NUV and FUV via Wiener deconvolution. In all cases, our focus was on determining the outermost slope of the galaxy, where PSF affects the profile (see Sec. 5.1.2). This was achieved by building broken exponential or single exponential models and replacing the cores of the models with Wiener images. The radius selected for joining Wiener cores with models depends on the model in question. In the case of broken exponential models, this radius is the break radius (except for NGC4321 and NGC5248, due to the low S/N of Wiener images). In the case of exponential models, this radius is the radius where the exponential function dominates the shape of the profile. The rationale behind utilising Wiener images as the cores of the models is to achieve the most accurate representation of how PSF spreads light from centre to the outskirts of galaxies (see Tab. 3.1 for details on models). Finally, in some galaxies where the PSF affects particularly cores of galaxies (in general, in cases of high inclination or the presence of a bright core), we substitute, after all the process, the Wiener core with the background subtracted image, in order to obtain a smoother profile in the inner parts.

Table 3.1: Models of galaxies for the PSF subtraction.

Name	Model (1)	h_1 [arcsec]		h_2 (2) [arcsec]		I_0 [counts s^{-1} pixel^{-1}]		R_J (3) [arcsec]
		NUV	FUV	NUV	FUV	NUV	FUV	
NGC1042	BE	75.62	65.10	17.39	16.5	2.58×10^{-2}	1.06×10^{-2}	156.0
NGC2712	BE	32.08	-	11.88	-	5.16×10^{-2}	-	85.5
NGC2903	BE	114.11	125.24	28.68	44.30	4.03×10^{-2}	1.03×10^{-2}	352.5
NGC3049	BE	24.77	19.37	6.31	5.03	7.97×10^{-2}	3.41×10^{-2}	82.5
NGC3198	BE/SE (4)	77.07	70.67	30.0	-	1.06×10^{-1}	2.53×10^{-2}	495.0 (5)
NGC3351	BE	68.13	84.25	23.07	19.71	6.61×10^{-2}	9.96×10^{-3}	210.0
NGC3368	BE	40.81	32.47	31.94	13.80	6.54×10^{-1}	5.34×10^{-1}	255.0
NGC3486	BE	62.69	54.85	14.04	10.81	1.20×10^{-1}	5.09×10^{-2}	195.0
NGC3596	BE	486.18	-	13.63	-	7.40×10^{-3}	-	111.0
NGC3972	SE	15.64	-	-	-	1.53	-	69.0
NGC4220	SE	30.16	12.86	-	-	2.28×10^{-2}	1.69×10^{-2}	54.0
NGC4307	SE	26.11	15.97	-	-	3.13×10^{-2}	1.11×10^{-2}	40.5
NGC4321	BE	52.99	49.22	11.60	13.09	1.89×10^{-1}	3.63×10^{-2}	400.0/234.0 (6)
NGC5248	BE	38.80	-	11.25	-	5.65×10^{-1}	-	330.0/243.0 (6)
NGC5866	SE	59.81	66.83	-	-	1.63×10^{-2}	5.96×10^{-4}	108.0
NGC5907	SE	42.45	46.40	-	-	9.98	1.00	345.0
IC3211	BE	11.07	10.93	4.76	3.0	7.53×10^{-2}	1.86×10^{-2}	37.5

(1): Broken exponential (BE) or Single exponential (SE)
(2): h_1 = inner BE slope or SE slope; h_2 = outer BE slope
(3): Radius where model is joined with the Wiener image, R_b for BE.
(4): In FUV a SE model was selected instead of a BE.
(5): In those models, it was decided not to join with the Wiener image, and R_J represents only the break radius.
(6): In these cases, the model is joined in a lower radius than R_b due to S/N of Wiener image. We present both values.

An example of this procedure comparing NGC3486 FUV profiles is presented in Fig. 3.5. In this particular case, we fitted a broken exponential model with $h_1 = 54.85''$, $h_2 = 10.81''$ and $R_b = 195''$, joining this model with the Wiener deconvolved image at $R = R_b$. This is one of the cases where the effect of FUV PSF on the outermost part of the profile is more clear. A summary of all this process (from the count maps to the PSF deconvolved intensity maps) can be found in Fig. 3.6.

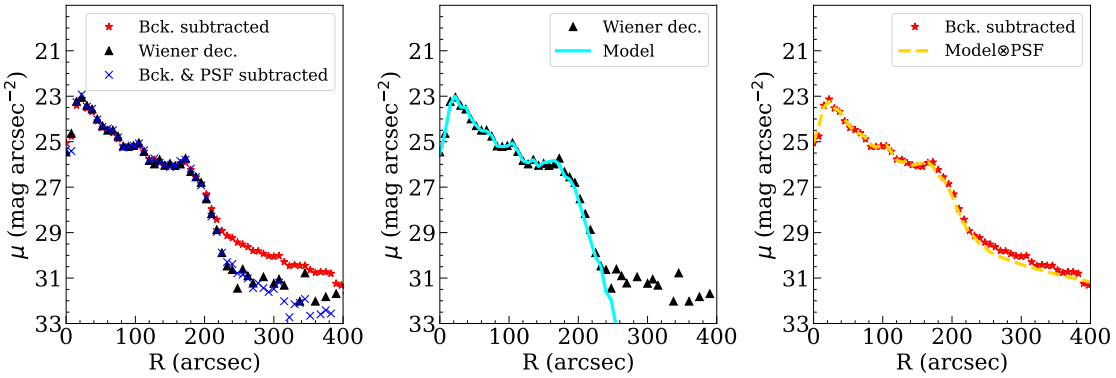

Figure 3.5: Example of the PSF subtraction applied to NGC3486 in FUV. Left panel shows the profile after background subtraction (red), profile from Wiener deconvolved image (black) and profile after applying all PSF subtraction (blue). Middle panel shows the model (cyan) fitted to the Wiener image, while right panel shows the model convolved with the PSF (yellow), among the background subtracted profile.

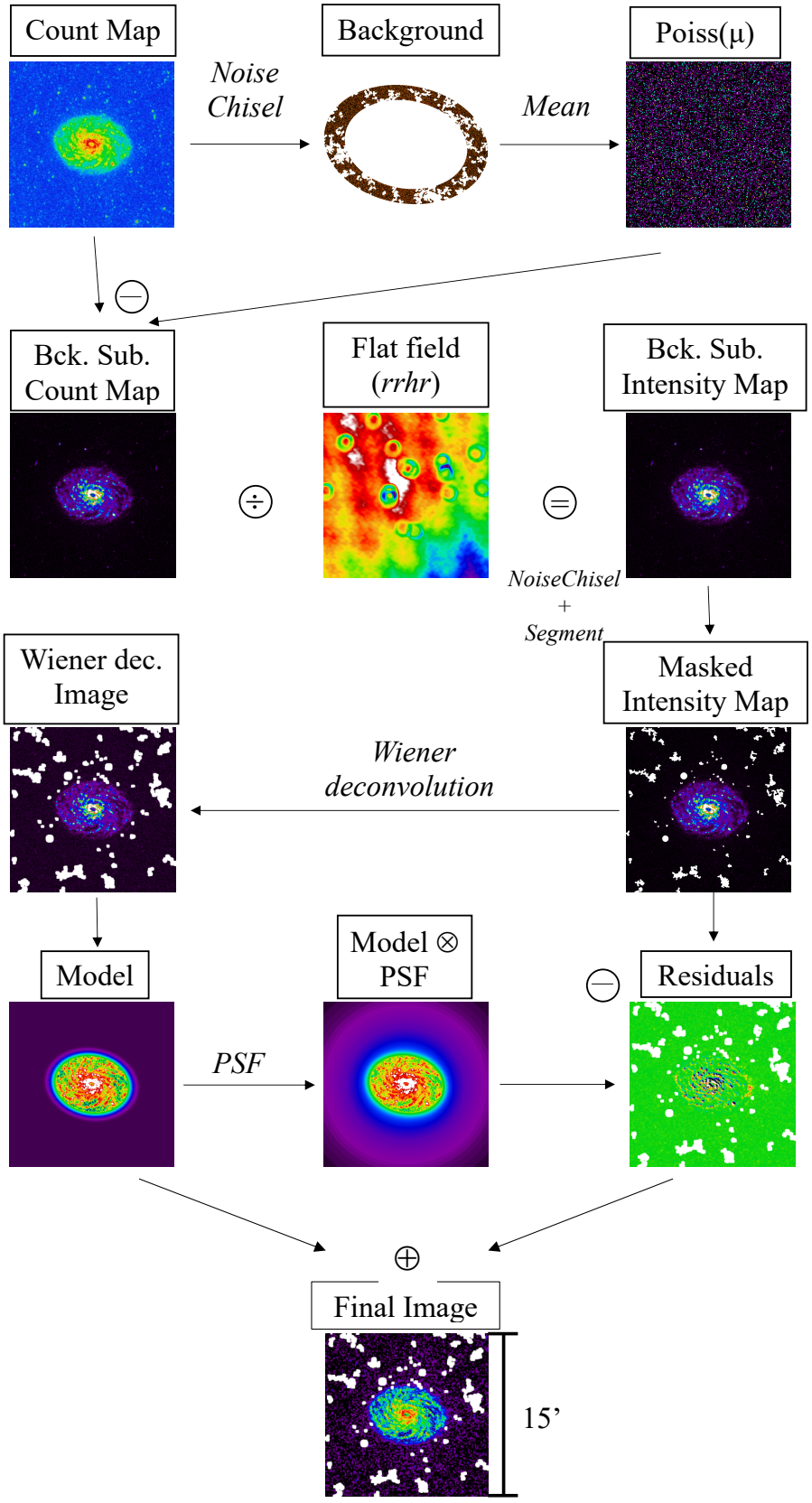

Figure 3.6: Scheme of the methodology applied for each galaxy, from the count map to the final background and PSF subtracted intensity map. In the figure, NGC3486 in FUV is used as example. Wiener deconvolved image, model, residuals and final image are smoothed for a better visualization.

Chapter 4

Results

4.1. Limiting surface brightness and magnitudes of our dataset

Following background subtraction and masking, we compute the images respective surface brightness limits and limiting magnitudes. To calculate the surface brightness limits we use GNUAstro's program MakeCatalog (Akhlaghi 2019b). We compute the surface brightness limits using the standard metrics for low surface brightness of 3σ fluctuations in equivalent areas of $10'' \times 10''$ (see, e.g., Trujillo & Fliri 2016). In contrast, magnitude limits are obtained by measuring the equivalent to 5σ background fluctuations in apertures (diameters) of $\varnothing = 2 \times \mathrm{FWHM}$ ($4''.2$ in FUV, $5''.3$ in NUV, Morrissey et al. 2007). As illustrated in Fig. 4.1 for NUV, and Fig. 4.2 for FUV, the reached surface brightness limits in the dataset following our background subtraction and source detection exhibit the expected dependence with $t_{exp}^{1/2}$ (a Pearson test returns p-values $< 1 \times 10^{-6}$), with values ranging from $\sim 28.5\,\mathrm{mag\,arcsec^{-2}}$ to $\sim 30.5\,\mathrm{mag\,arcsec^{-2}}$.

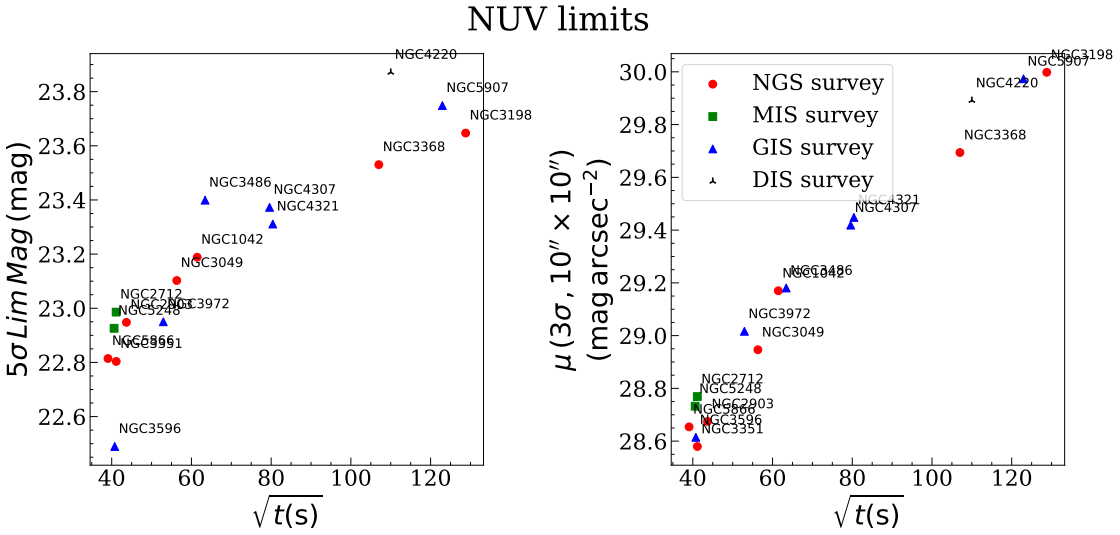

Figure 4.1: 5σ limiting magnitude (diameter of the aperture=$2 \times$ FWHM) and 3σ surface brightness limit ($10'' \times 10''$ area) as a function of exposure time in the NUV images.

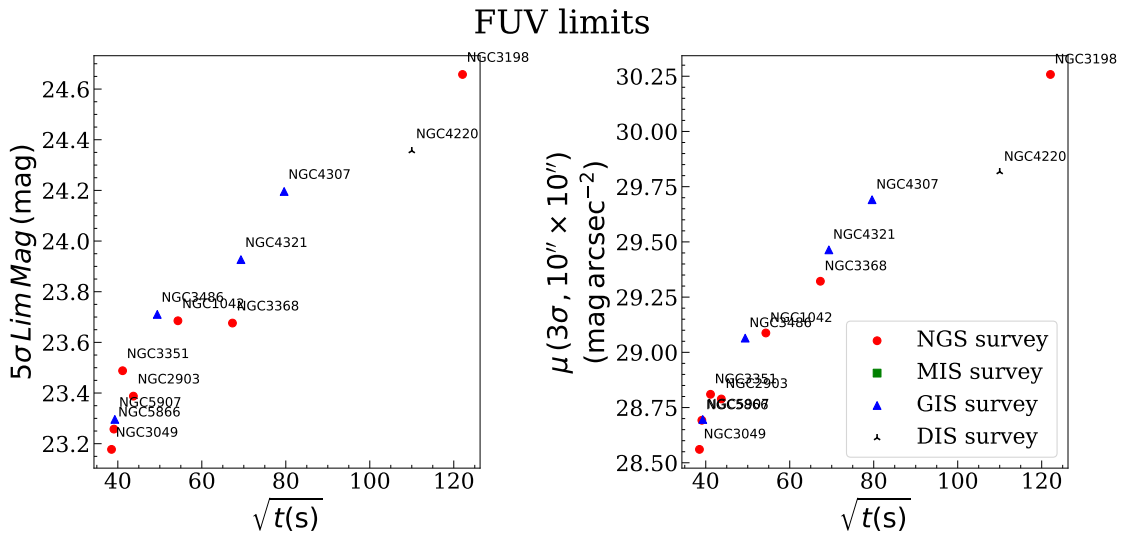

Figure 4.2: Same as Fig. 4.1 for FUV images.

4.2. Surface brightness and Colour profiles

The ellipticity and position angles derived from LIGHTS LBT-g images (Tab. 2.1) are used to compute the UV surface brightness profiles of galaxies and, in those cases with FUV, $(FUV - NUV)$ profiles. To this end, we measure the sigma-clipped surface brightness in elliptical annuli of widths 1.5″, 3″, 4.5″ or 7.5″, depending on the apparent size of the galaxy, using the GNUAstro's script astscript-radial-profile (Infante-Sainz et al. 2024). In the cases of NGC3972, NGC4220, NGC4307, NGC5866 and NGC5907, where the inclination is particularly high, the profiles are computed using wedge-like shapes centred on the major axis, with apertures of ±5° (±3° in NGC5907). All surface brightness profiles are plotted only where they are above $3 \times \sigma_{bck}$, i.e., when the surface brightness is above the limitting 3σ surface brightness at the area of the annuli. The uncertainties are calculated by taking the square sum of each annulus standard deviation, with σ_{bck} divided by the square root of the area of the annulus.

The colour profiles are plotted only where FUV surface brightness is above the surface brightness limit (since FUV is generally the band most affected by this limitation). Colours are corrected for Galactic extinction using Cardelli et al. (1989) extinction curves for the Milky Way, resulting in $E(FUV - NUV) = 0.11E(B - V)$ (see Bianchi et al. 2017). The optical extinctions $(E(B - V))$ are obtained from Zaritsky et al. (2024).

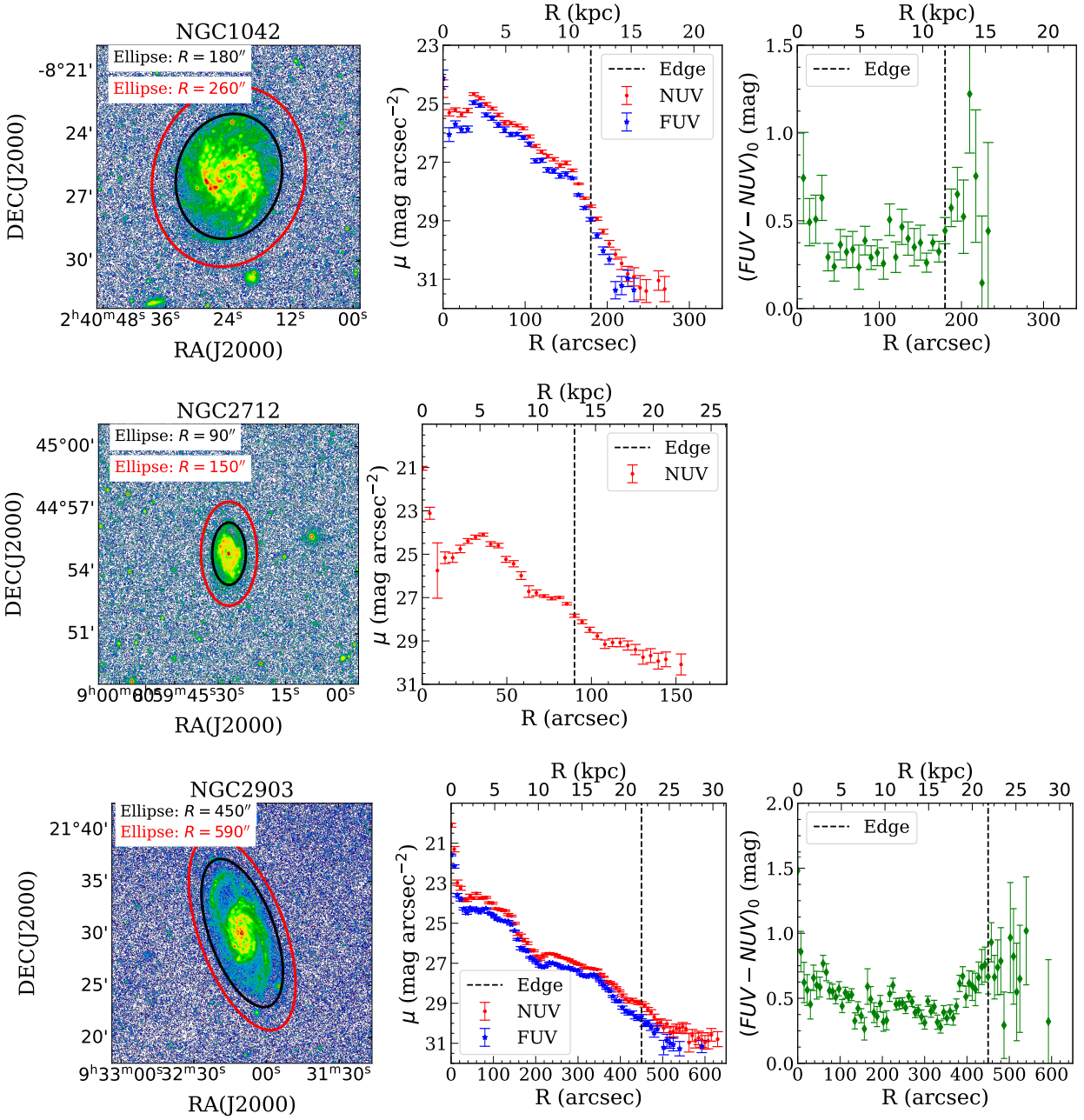

Figure 4.3: Left panel: NUV background subtracted images. Middle and right (if applicable) panels: surface brightness and colour (corrected from Galactic extinction) profiles. The red ellipses represent where colour profiles are stopped (NUV surface brightness profiles only if there is no colour profile). Black ellipses represent the edges of the galaxies according to the criteria described in Trujillo et al. (2020) (see Sec. 4.2) . The radial location of those ellipses are also represented as dashed vertical lines in the profiles.

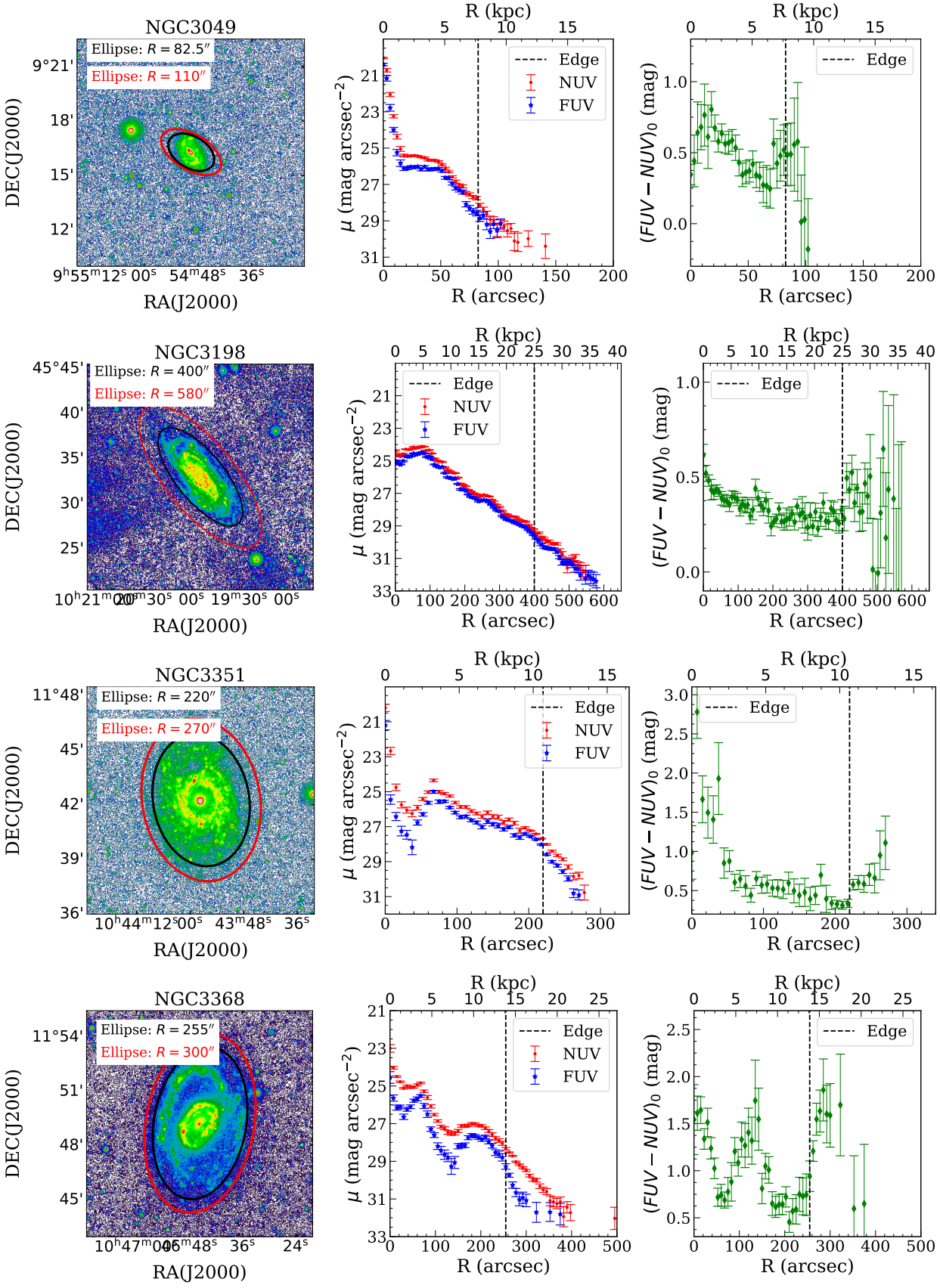

Figure 4.3: Profiles (cont.)

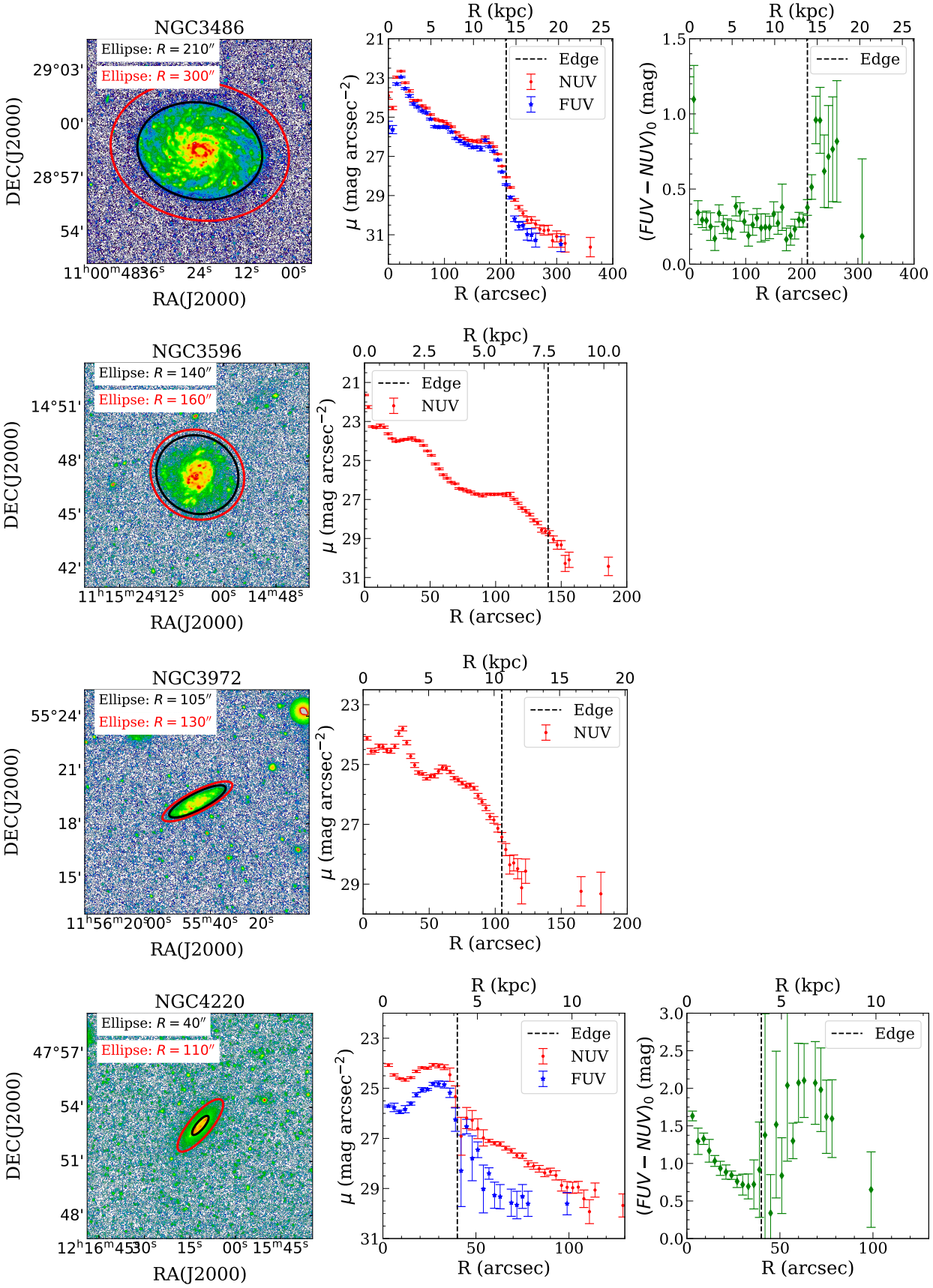

Figure 4.3: Profiles (cont.)

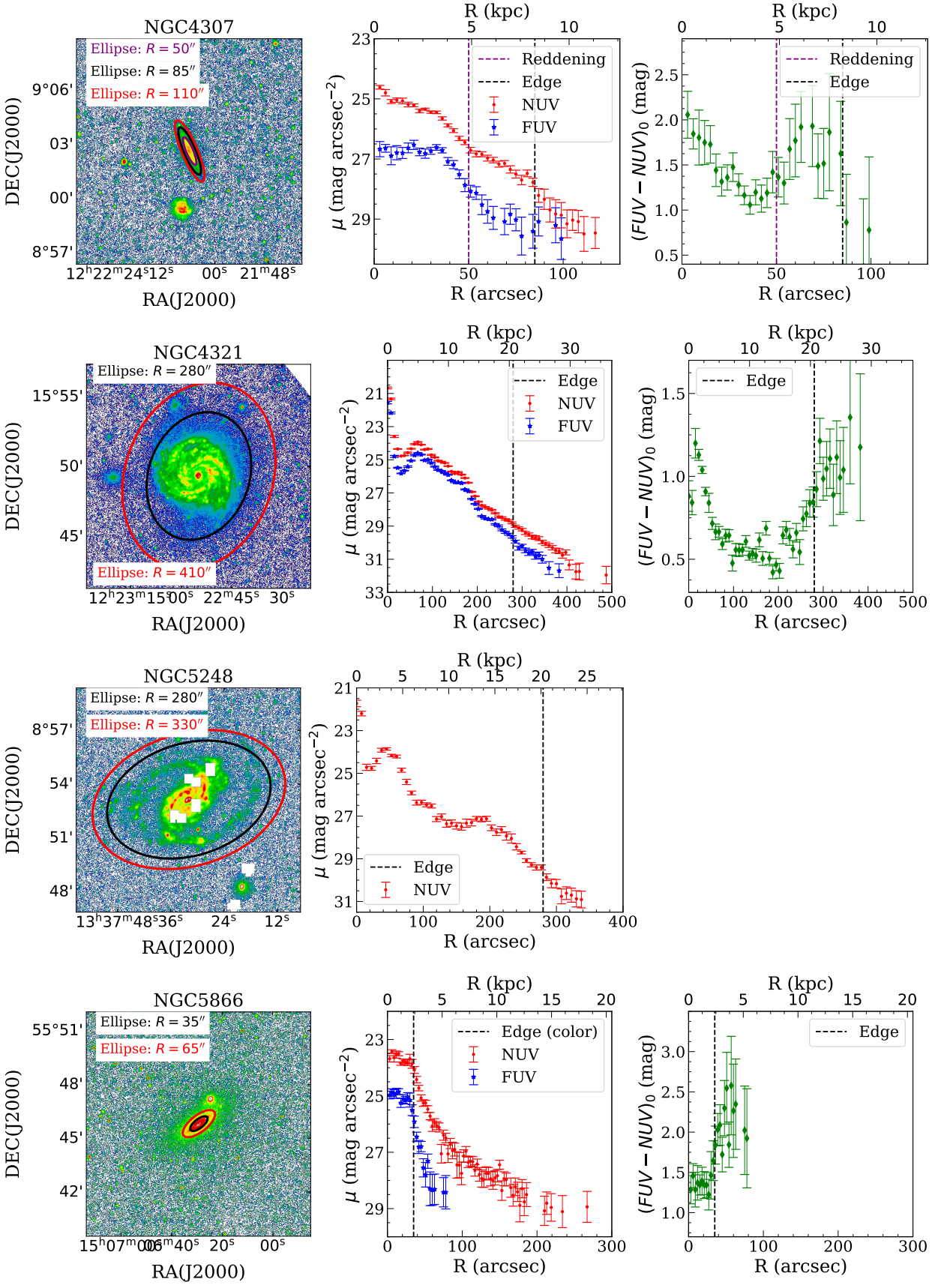

Figure 4.3: Profiles (cont.)

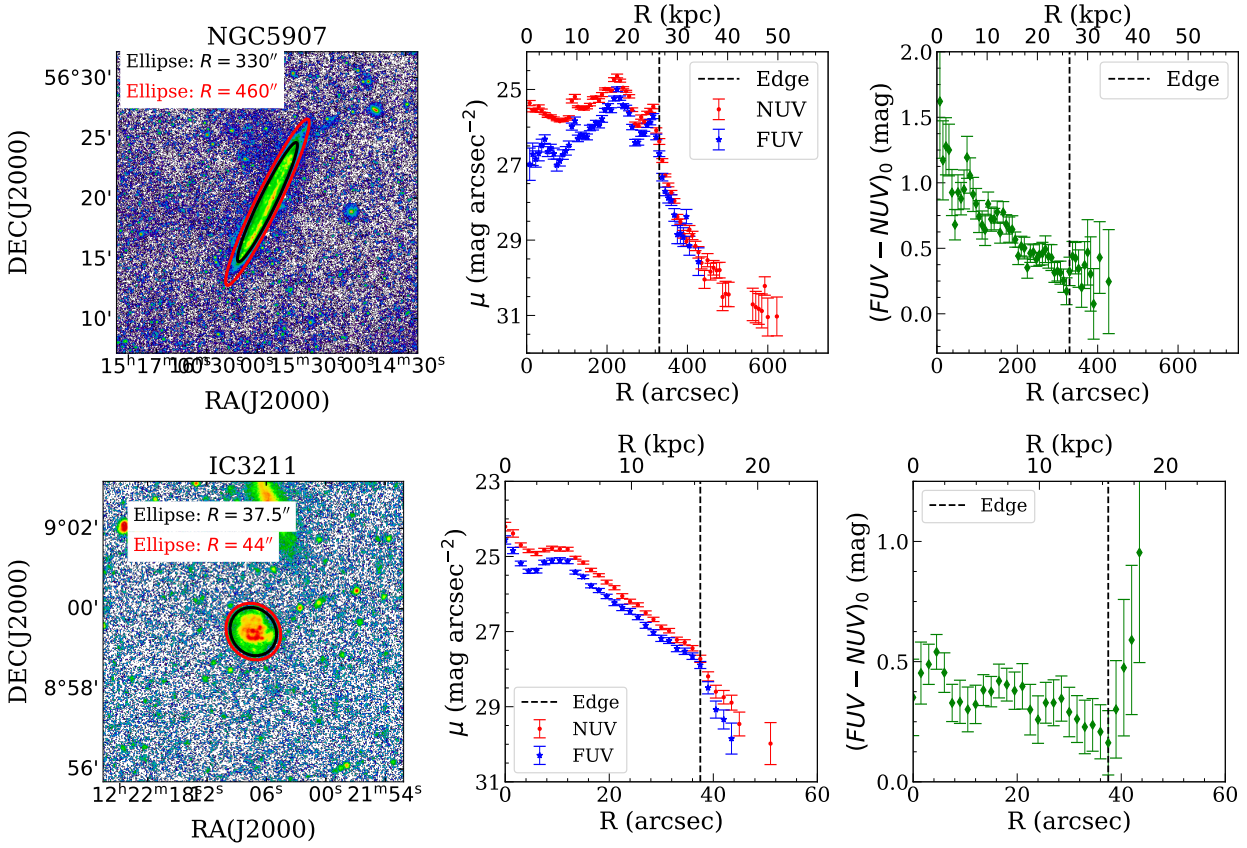

Figure 4.3: Profiles (cont.)

In Fig. 4.3 we also present as black ellipses the radius where we identify an edge. This identification of the edge is based on the procedures outlined by Trujillo et al. (2020) and Chamba et al. (2022): the outermost change in the slope on the surface brightness profiles, indicative of the star formation threshold (past or present) of the disk. The feature coincides with the reddening at the end of the $FUV - NUV$ profile for those galaxies where FUV and NUV are available. When both criteria are applicable, the edge location is constrained by the colour profile, with the surface brightness profiles then examined to ascertain whether this reddening is situated at the change of slope. Subsequently, the NUV (and FUV) images, among the optical images, are examined to check whether this edge is correlated with the visual border of the galaxy.

This criterion enables the identification of a clear edge in 13 galaxies ($\sim 76\%$), which are in agreement with the visual borders observed in the images. There are 4 galaxies though which have no clear edge locations due to the presence of different features. In the case of NGC3198, we detect a reddening at $400''$ that correlates with the visual apparent end of the galaxy, while another edge is possibly located at $520''$ according to the surface brightness profiles, but limited by signal-to-noise in the colour profile. A comparable situation is observed in NGC4307, where the reddening begins at $50''$ while an edge is identified in the NUV profile at $85''$. At this point, the colour profile is significantly constrained by the FUV depth. In the case of NGC5907, there is a clear truncation in both the FUV and NUV surface brightness profiles at $330'' = 26.40$ kpc (in agreement with the reported truncation by Martínez-Lombilla et al. 2019). However, we also report a possible new feature at $420''$ observed in the NUV surface brightness profile, wich is again limited by FUV depths. Nevertheless, we set the first truncation as the edge of the galaxy (see Sec. 5.2.1 for more details). Finally, in the case of NGC4321 we report a possible truncation at $280''$ that does not correspond entirely with the extension of the galaxy as observed in NUV and optical images.

Table 4.1: R_{edge} reported in Fig. 4.3, among the criteria selected for the location of the edge: surface brightness truncation (1) and/or colour reddening (2). Uncertainties are based on the step of profiles.

Name	R_{edge} [″]	R_{edge} [kpc]	Criteria
NGC1042	180.0 ± 7.5	11.78 ± 0.49	1,2
NGC2712	90.0 ± 4.5	13.18 ± 0.66	1
NGC2903	450.0 ± 7.5	21.82 ± 0.36	1,2
NGC3049	82.5 ± 3.0	7.72 ± 0.28	1
NGC3198	400.0 ± 7.5	25.02 ± 0.47	2 - 1
NGC3351	220.0 ± 7.5	10.67 ± 0.36	1,2
NGC3368	255.0 ± 7.5	13.85 ± 0.41	2
NGC3486	210.0 ± 7.5	13.85 ± 0.49	1,2
NGC3596	140.0 ± 3.0	7.67 ± 0.16	1
NGC3972	105.0 ± 3.0	10.59 ± 0.30	1
NGC4220	40.0 ± 3.0	3.94 ± 0.30	1,2
NGC4307	85.0 ± 3.0	8.24 ± 0.29	1
NGC4321	280.0 ± 7.5	20.63 ± 0.55	1
NGC5248	280.0 ± 7.5	20.23 ± 0.54	1
NGC5866	35.0 ± 3.0	2.39 ± 0.21	1,2
NGC5907	330.0 ± 7.5	26.40 ± 0.60	1,2
IC3211	37.5 ± 1.5	15.45 ± 0.62	1,2

Chapter 5

Discussion

5.1. Comparison with GALEX pipeline

In this work, we have presented an analysis of GALEX UV data based on a methodology optimised for low surface brightness studies. However, the GALEX archive also includes data products with a background subtraction and object detection pipeline which are, in principle, suitable for subtracting the radial and colour profiles of Sec. 4.2. The pipeline is described in detail in Morrissey et al. (2007). In the following sections, we compare the results of the GALEX pipeline (referred to henceforth as GALPIP) with our methodology. To this end, we utilise the background-subtracted intensity maps (*-intbgsub*) of the galaxies, placing our own mask in order to compare as many of the same sources of light as possible. In this section, we will present the cases where the differences are most notable, due to background (Sec. 5.1.1) or due to PSF effects (Sec. 5.1.2). The full set of differences for all galaxies between different methods is presented in Appendix. A.

5.1.1. Effects of mask and background

In Sec. 3.1, we have presented a methodology for background subtraction and source detection based on the GNUAstro tools and a global determination of the background as a Poisson distribution. This methodology differs from that presented in Morrissey et al. (2007). In the GALEX pipeline, while a Poisson distribution is also considered for the background, this is determined locally in large bins ($192''$ each, as described in Morrissey et al. 2007, Sec. 3.3) and based on SExtractor source detection (Bertin & Arnouts 1996). The disparate methodologies employed in background subtraction and source detection may account for the discrepancies observed between GALPIP profiles and those obtained by us after background subtraction (hereafter called *UV LSB*).

Upon examination, it was observed that the GALPIP profiles exhibited a diminished brightness in the outer regions relative to the *UV LSB* ones. Given the methodology employed for the acquisition of these images, it can be concluded that GALPIP images exhibit a higher degree of background subtraction than those produced by our own methodology. In order to ascertain which estimation of the background is more accurate, we have analysed four galaxies with the greatest discrepancy. The following galaxies were selected for analysis: NGC2903, NGC3198, NGC3368 and NGC4321. Fig. 5.1 presents a comparison between the GALPIP and the *UV LSB* profiles for the four aforementioned galaxies.

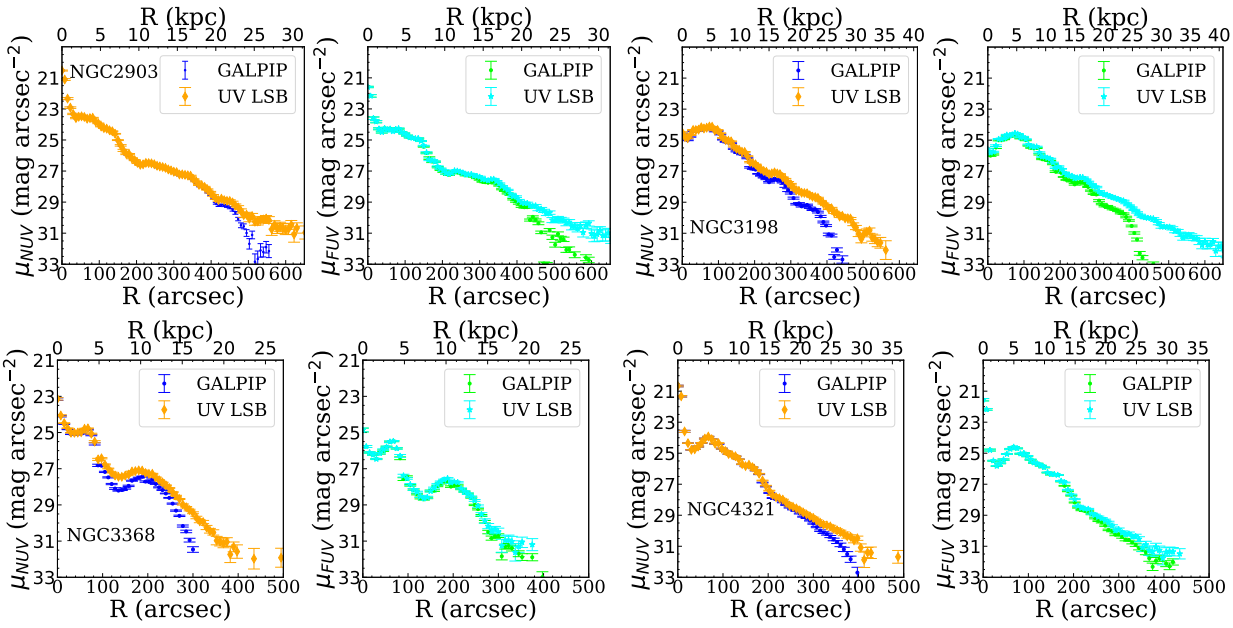

Figure 5.1: Comparison between GALPIP profiles and our profiles after background subtraction (*UV LSB*). In each galaxy, right panel is FUV and left panel is NUV.

Given that the differences are greater in NUV, and that in FUV only NGC2903 and NGC3198 present differences and at same level as NUV, we focus on NUV. The initial step is to analyse the asymptotic value of the end of the profile. If the data has been properly masked, and the background has been well subtracted, the profile (in units of counts) should approach to 0 when observed far enough from the galaxy. This is not the case for GALPIP profiles, where NUV presents profiles with asymptotic values of -0.19 ± 0.04, -0.93 ± 0.31, -0.25 ± 0.20 and -0.36 ± 0.13 counts in NGC2903, NGC3198, NGC3368 and NGC4321 respectively. These findings already indicate the presence of consistent negative backgrounds in GALPIP in the vicinity of the galaxies, values that, when converted to magnitudes, may obscure low surface brightness structures (see Sec. 5.2 for an example in NGC3198).

In order to ascertain the underlying reasons for these different backgrounds, it is necessary to examine the background maps of GALPIP (*-skybg* in GALEX archive). In the cases of NGC3198 and NGC3368, the background maps clearly illustrate the causes of these differences. Figs. 5.2 and 5.3 present the background in the region of the galaxy. The figures show the presence of a structure in the background at the centre of the galaxy. In other words, the galaxy (probably its scattered light due to the PSF effect) is influencing the background estimation by increasing it.

The rationale behind these structures is not entirely clear, although they may be linked to the object masks used for measuring the background. In the recent years, as low surface brightness astronomy has become a subject of intense study, the importance of source detection and background estimation has become increasingly apparent. These processes represent a crucial step in the analysis of data. Consequently, the implementation of a robust source detection pipeline and a well-defined strategy for background determination is of paramount importance in these studies (see, for example, Kelvin et al. 2023; Watkins et al. 2024). In the case of NGC3198 and NGC3368, the source detection maps (Fig. 5.4) of GALPIP do not cover the full observed galaxy. This could be the reason why galaxies are affecting the background estimation. Furthermore, our methodology involves measuring the background at a sufficient distance from the galaxy to minimise the potential for internal scattered light due to the galaxy itself. Additionally, we consider a flat background (a Poisson distribution with the same mean value) around the galaxy and employ a more aggressive mask to prevent the presence of structures in the background.

The cause of background over-subtraction in NGC2903 and NGC4321 by GALPIP remains less clear. Upon examination of the GALPIP background maps, no discernible structure is evident in the vicinity of

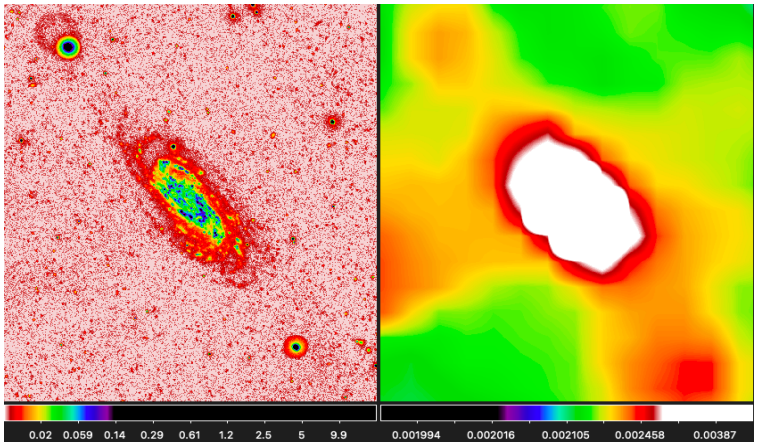

Figure 5.2: SAOImageDS9 capture of NUV NGC3198 intensity map (left) and background from GALPIP in the same region (right). The contrast is leveled to see the full galaxy and appreciate the structure in background.

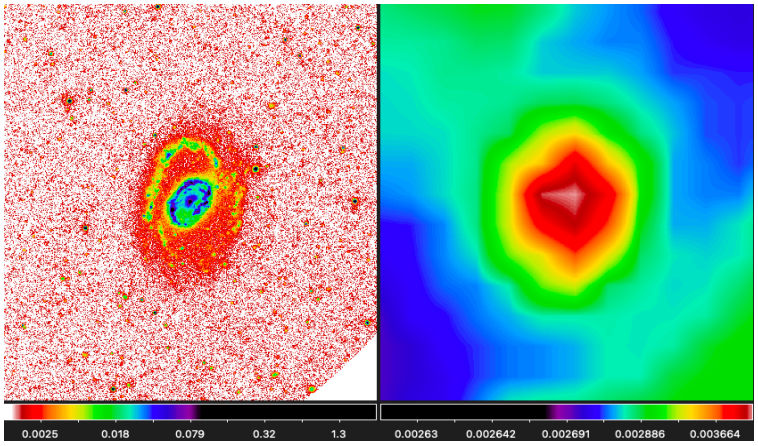

Figure 5.3: SAOImageDS9 capture of NUV NGC3368 intensity map (left) and background from GALPIP in the same region (right).

the galaxies. Nevertheless, some discernible structure is observed in the full background map. An annulus is observed around the centre of the image, where the background is lower than at the centre and in the outer part of this annulus. As illustrated in Fig. 5.5, NGC2903 and NGC4321 fall in a transitional zone between lower (green-yellow) and higher (red-white) background levels. Accordingly, the GALPIP profiles are combining in the same radius pixels where the background is higher than other pixels, resulting potentially in this over-subtraction. The reason for the presence of this annulus is not clear. However, it is present in other backgrounds and does not affect the galaxies.

We are not the first on criticising the GALPIP backgrounds. In fact, Bianchi et al. (2014) recommends that a method of careful background subtraction should be considered in extended galaxies, given that UV-emission peaks of such galaxies are identified as individual sources within the GALEX pipeline. Other works utilising GALEX data, such as that presented in Gil de Paz et al. (2007), adopt a more conventional approach to background subtraction, whereby the background is measured as the mean of regions devoid of sources and situated at a sufficient distance from the galaxy to prevent contamination. The novel aspect of our methodology is that we combine both philosophies in order to reach the deepest surface brightness possible:

1. The background is characterised by the mean of source-masked regions around the galaxy. This methodology allows us to avoid background structures that are observed in Figs. 5.2 and 5.3. It is

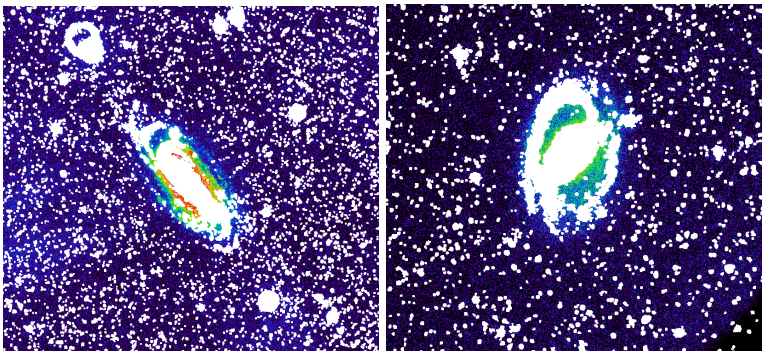

Figure 5.4: NGC3198 (left) and NGC3368 (right) NUV count maps masked with the *-objmask* files available in GALEX archives.

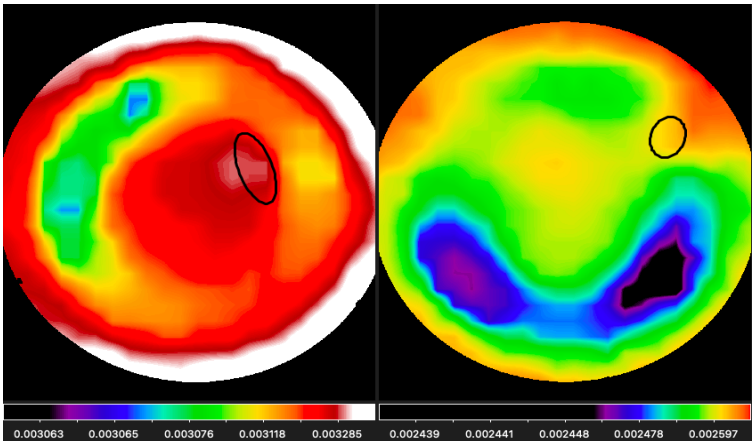

Figure 5.5: NGC2903 (left) and NGC4321 (right) NUV background maps from GALPIP. Galaxies are represented by a black ellipse of $R = R_{edge}$ (see Tab. 4.1).

therefore assumed that the field of the galaxy exhibits no significant gradients in the background. This was validated by measuring the background in different positions around the galaxy and comparing the obtained values. Following these tests, it was determined that a global mean value could be safely considered for each galaxy.

2. Rather than subtracting the background as a constant value, a random 2D Poisson distribution is subtracted based on this value, resulting in a pseudo-Gaussian background centered on 0. This does not affect the value of background in principle, as the mean of the Poisson distribution after subtracting the background value is 0 (i.e., $\mu_2(P_\lambda - \mu_1) = 0$, where μ_1 is the mean of P_λ). However, as previously noted, source detection plays a pivotal role in low surface brightness analysis. Software such as NoiseChisel has been designed for the detection of faint sources, but assumes a Gaussian background in its detection algorithms. Consequently, the optimal functionality of these programs is achieved when a Gaussian background is employed.

The combination of both strategies allows us to obtain surface brightness depths of 3σ in $100\,\mathrm{arcsec}^2$ of $\sim 28.5 - 30.5\,\mathrm{mag\,arcsec}^{-2}$ (see Fig. 4.1, 4.2). These depths, applied as limits to the data, result in profiles that reach values from $\sim 29\,\mathrm{mag\,arcsec}^{-2}$ to $\gtrsim 31\,\mathrm{mag\,arcsec}^{-2}$ in the case of the deepest data (e.g., NGC3198). Comparing these results with other papers is difficult, as there is no clear value for the surface brightness limit, and each work has its own criteria for limiting the profiles. Bianchi (2011) report sensitivities of $\sim 27.5\,\mathrm{mag\,arcsec}^{-2}$ for exposure times $\approx 1500\,\mathrm{sec}$, but do not specify which metrics they are using. However, with similar exposure times, we get depths of $\sim 28.6 - 28.8\,\mathrm{mag\,arcsec}^{-2}$ (see Tab. 2.1), about 1 mag deeper. Gil de Paz et al. (2007) shows profiles for the NGS survey galaxies that reach depths of $\sim 29 - 30\,\mathrm{mag\,arcsec}^{-2}$, but their profiles are limited by the level of the background, or the error in

NUV surface photometry. However, we can make a direct comparison for NGC1042, wich is present in both works. In Gil de Paz et al. (2007), the surface brightness profile in both FUV and NUV reaches a depth of 29 mag arcsec^{-2}, while in our case the profile stops at 31 mag arcsec^{-2}, 2 mags deeper. Bouquin et al. (2018), following the strategy of Gil de Paz et al. (2007), present surface brightness profiles of 1931 galaxies in FUV and NUV reaching depths of $\sim 30/29$ mag arcsec^{-2} respectively (see Fig. 3 of their paper), while we are able to obtain profiles down to ~ 31 mag arcsec^{-2} in both bands in $\sim 50\%$ of our sample (see Fig. 4.3). Finally, Chamba et al. (2022), where low surface brightness features are taken into account, report a depth in the GALEX images used in their paper of 29.6 ± 0.5 mag arcsec^{-2}, in the range we report in this work.

5.1.2. Effects of PSF

In the previous section, we discussed the differences between our methodology for background subtraction and source detection methodology and the GALPIP results, and explained the source of these differences. However, taking into account the effect of the PSF on the galaxy profiles (explained in Sec. 3.2), more differences appear, especially in the colour profiles of some galaxies. In Fig. 5.6, we show 6 cases where the colour profiles, after the PSF subtraction, present significant differences with both the GALPIP and our background subtracted images. For these galaxies, the difference is the same: after the PSF subtraction, the colour profiles at the outermost parts of the galaxies become redder, with the transition between the flat part and this reddening located around the edge of the galaxy (see Sec. 4.2). In this section we will show how these differences are explained by the PSF, and why it is key to take these effects into account.

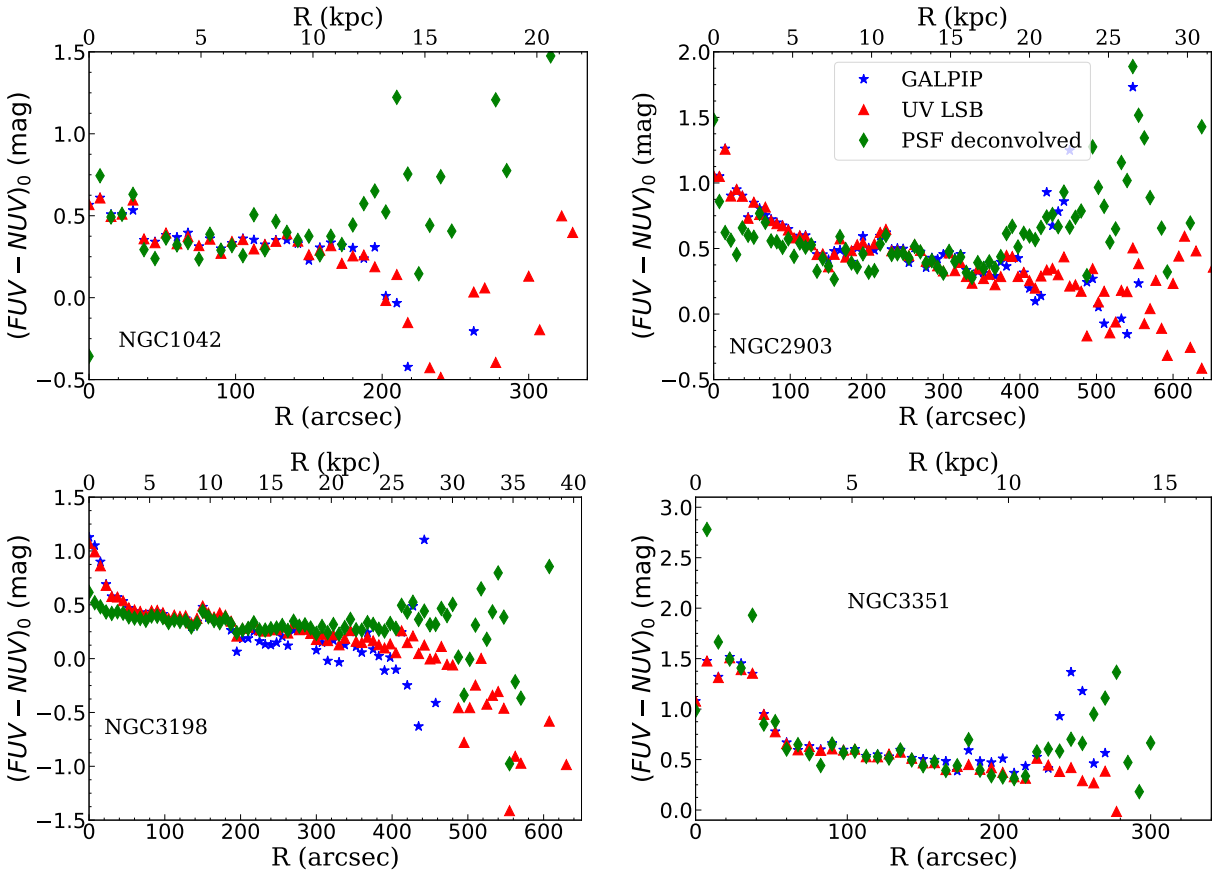

Figure 5.6: Comparison between GALPIP (blue), ours after background subtraction (*UV LSB*, red) and PSF subtracted (green) colour profiles of 6 galaxies of the sample.

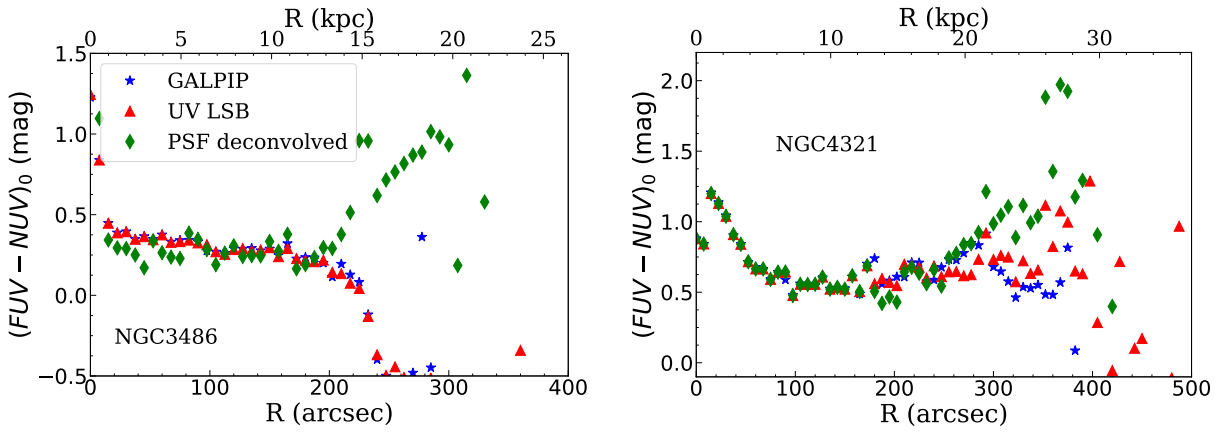

Figure 5.6: Cont.

To analyse the effect of the PSF, we focus on the galaxy that seems to have the largest effect, NGC3486. In Fig. 5.7 we show the differences in the NUV, FUV and colour profiles. As observed in the profiles, the results are similar in all three methods in the inner 200″, with a break at $\sim 195''$. However, in the GALPIP and *UV LSB* FUV profiles a potential second break appears at $\sim 220''$, with an outer profile that decays more slowly until the surface brightness limit of the image. Since this feature is not observed in NUV, the resulting colour profile shows a rapid drop to negative $(FUV - NUV)$ colours beyond 220″. In contrast, once the PSF effects are taken into account, the FUV has a similar behaviour to the NUV, and the colour profile shows a reddening beyond the break radius.

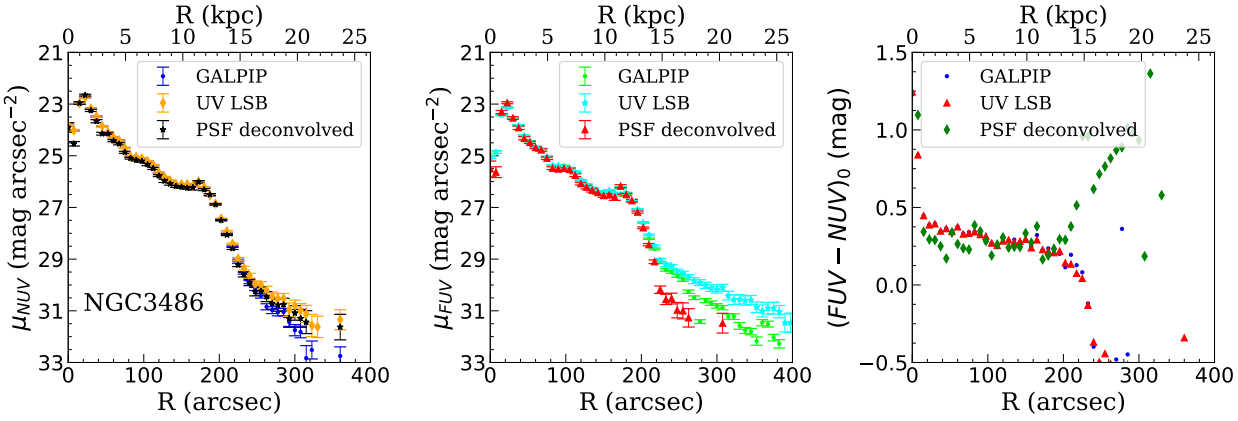

Figure 5.7: Comparison between GALPIP, *UV LSB* and PSF subtracted results for NGC3486. *Left:* NUV surface brightness profile. *Middle:* FUV surface brightness profile. *Right:* $(FUV - NUV)_0$ colour profile, corrected from Galactic extinction.

According to Fig. 5.7, the effect of the PSF is particularly relevant in FUV profiles. This is explained by the shapes of the PSFs in the outer regions. As shown in Morrissey et al. (2007), FUV and NUV PSFs have different behaviour. While FUV follows a classic Moffat profile, NUV has a quick drop at $\sim 40 - 50''$ followed by a recovery to a power-law tail. This quick drop in the NUV PSF (see Fig. 3.3 or 3.4) has an effect on the colour profile of the PSFs. In Fig. 5.8, we show the intensity and colour profiles of the PSF created in Sec. 3.2. Looking at the colour profile, we can see that the drop in the NUV PSF at $\sim 40''$ causes the colour profile to quickly become bluer around this point.

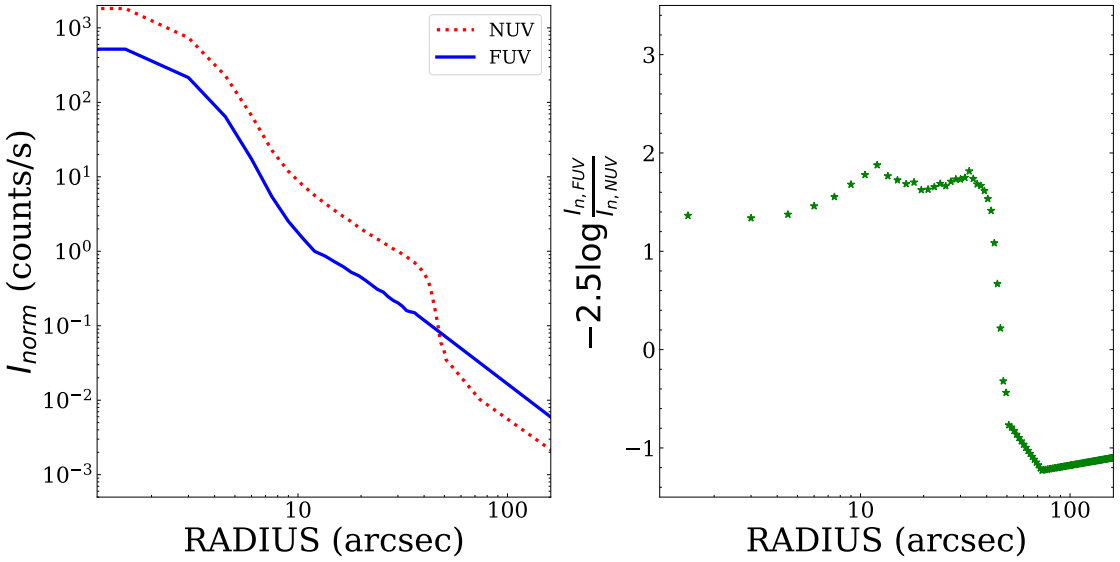

Figure 5.8: NUV and FUV PSF profiles normalized as explained in Sec. 3.2 (to the vaule at $R = 30''$ in NUV and at $R = 12''$ in FUV, *left*), and colour profile of the PSF (*right*).

Interestingly, the shape observed in the colour drop is similar to that observed in the colour profile of NGC3486 without considering PSF effects. It is therefore reasonable to assume that the colour drop in the galaxy is related to the effect of the PSF. To see this, we can study what is the effect of convolving the PSFs with the model of the galaxy. Consider a broken exponential model for NGC3486, with a break at $195''$ and slopes of $h_1 = 62.69''$, $h_2 = 14.04''$ for NUV, and $h_1 = 54.85''$, $h_2 = 10.81''$ for FUV. These models are based on the Wiener deconvolved images as explained in Sec. 3.2. In Fig. 5.9 we show surface brightness and colour profiles of these models before and after the convolution with the PSF.

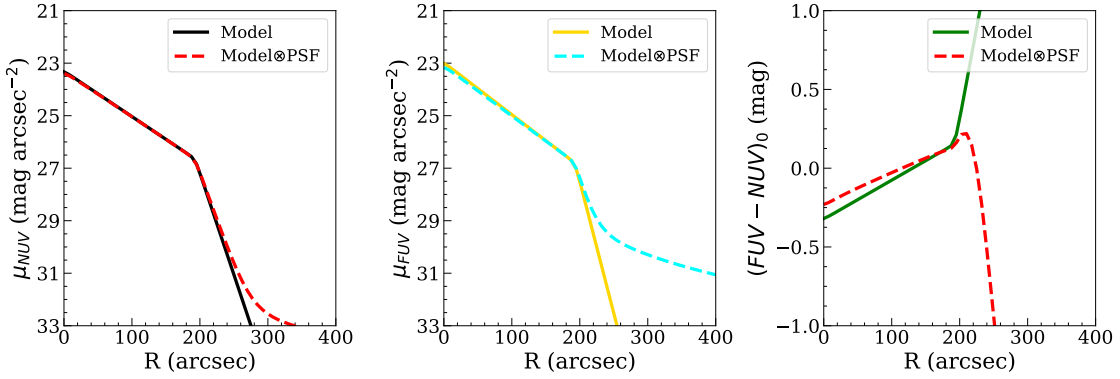

Figure 5.9: Comparison between broken exponential models based on NUV and FUV of NGC3486, with their convolution with PSFs. *Left:* NUV surface brightness profile. *Middle:* FUV surface brightness profile. *Right:* $(FUV - NUV)_0$ color profile.

The surface brightness profile of the FUV model convolved with the PSF clarifies what is happening to the profiles. For a broken exponential model such as NGC3486 FUV, the PSF not only makes h_2 higher (i.e., the profile decays more slowly), but also dominates the profile beyond $\sim 29\,\mathrm{mag\,arcsec^{-2}}$. Since the tail of the FUV PSF is brighter than the NUV according to Fig. 5.8, this also causes the effect of the PSF to appear at brighter surface brightness, resulting in the drop in the colour profile at around the break radius.

We can also check the accuracy of the FUV models convolved with the PSF by comparing them with

the original images. In Fig. 5.10, we show the comparison between the *UV LSB* FUV and model profile for 3 of the galaxies from Fig. 5.6: NGC1042, NGC2903 and NGC3486. In all three cases we can see that the model, when convolved with the PSF, is able to nearly reproduce almost the profile of the galaxy at the end, where the PSF effect shows significantly. In the lower panels it is more clear: the difference between model and data is close to 0.

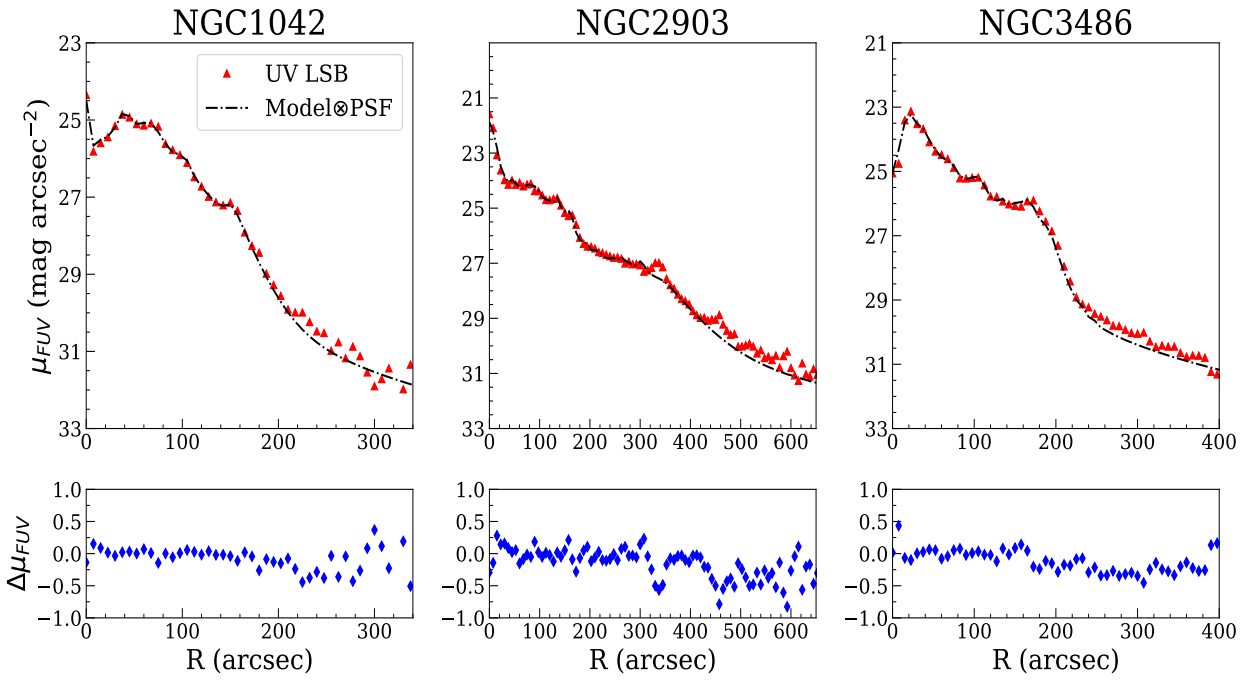

Figure 5.10: Comparison between *UV LSB* surface brightness profile and the model convolved with the PSF for three different galaxies. Bottom pannels show the difference between both profiles defined as $\Delta\mu = \mu_{original} - \mu_{model}$.

Note that the correct treatment of the PSF in the profiles is crucial for the interpretation of the results at the end of the galaxies, especially in the colour profiles. Looking at the red profiles in Fig. 5.6, it is clear that not subtracting the PSF effects makes the colour profiles bluer at the end of the profiles, with the particular cases of NGC1042, NGC3351 and NGC3486 also becoming negative. Assuming that this colour shape is real and not an effect of the PSF, it would be contrary to what has been observed in other galaxies at optical wavelengths. For Type II galaxies with a broken exponential profile, such as NGC1042 or NGC3486 (steeper in the outer parts, flatter in the inner parts), several papers have shown that the colour profiles become redder beyond the break radius. For example, Bakos et al. (2008) presented this feature for nearby late-type galaxies in the SDSS, while Azzollini et al. (2008) derived similar results for *HST* galaxies at $0.1 \leq z \leq 1.1$. Using simulations, Roškar et al. (2008) explained this reddening as a result of the interplay between a radial star formation cut-off and a redistribution of the stellar mass, with their models suggesting that the main younger stars are located at the break radius, with older stellar populations beyond due to migration. Since the GALEX FUV-NUV color is extremely sensitive to young stellar populations (Bianchi 2011), it would be reasonable to expect this reddening beyond the break radius also in Type II galaxies such as NGC1042 or NGC3486. The PSF subtraction applied in this work thus reconciles the observed GALEX FUV-NUV shape with that expected from theories of star formation in late-type galaxies.

Finally, note also the importance of a proper background subtraction when investigating PSF effects. Since these effects appear at the faint end of the profiles, an oversubtraction of the background can mask the effect of the PSF. For example, in NGC2903 the background is oversubtracted in both bands in GALPIP (Fig. 5.1), but then looking at the colour profile it is not so clear whether there is a reddening or a fading, due to the over-subtraction in NUV. With our methodology, however, there is a clear difference when subtracting

the PSF (interestingly, the FUV profile when subtracting the PSF is close to that of GALPIP).

5.2. Interpretation of the profiles

In the previous section, we have discussed the accuracy of our method compared to previous works, and the importance of considering the effects of the PSF when studying the faint end of the galaxies. In this section, we give a qualitative analysis of the PSF subtracted profiles (Fig. 4.3). We focus this analysis on the detection of low surface brightness features in the profiles of some galaxies, and the reliability of the edges presented in Tab. 4.1.

5.2.1. Detection of edges

As mentioned in Sec. 4.2, we have adopted the methodology detailed in previous works (Trujillo et al. 2020; Chamba et al. 2022) to detect possible edges, R_{edge}, in our profiles. In the particular case of the UV, these edges, which are thought to be related to the end of the in-situ star formation in the discs, should be more easy to spot. In general, we identify a clear edge in $\sim 76\%$ of the sample. In the cases of clear Type II galaxies with colour profiles (NGC1042, NGC3351, NGC3486 and IC3211) the detection of the edge is based on the observed break in the surface brightness profiles and the reddening in the colour profiles. In the four cases, the identified radial location of the edge also matches the visual edge in NUV images.

In the case of NUV-only galaxies (i.e., those where colour information is not available) with a clear Type II profile, we are also able to detect the edge, but only using the break in the surface brightness profile as a selection criterion. Such are the cases of NGC2712, NGC3596, NGC3972 and NGC5248. In the first galaxy, the break is particularly clear at $\sim 90''$ after a flat part on the profile. This flat part is caused by the outermost arm at the top of the galaxy. For NGC3596, unless there is a first break at $\sim 110''$, we detect a second break at $\sim 140''$. This further break seems to be related to an arm in the lower, western part of the galaxy, which is particularly asymmetric along the major axis (note that opposite to this arm, i.e., in the upper, eastern part, there is no light from the galaxy around the located edge; this could be related to the presence of a first break in the profile). In the cases of NGC3972 and NGC5248, there is a single break in the outermost part, close to the surface brightness limit of the images, but still observable. In the 4 cases, the detected breaks correlate with the apparent boundary in the images.

For other galaxies, the correlation between the reddening point and a break in the surface brightness profiles is less clear. In the cases of NGC2903 and NGC3049, the break is more clearly observable in the NUV profiles, and the reddening at this point is noticeable but highly affected by the noise (especially in NGC3049). In fact, in NGC2903 the break at $R_{edge} = 450''$ is further away in NUV than the reddening (about $10''$). This seems to be related to an arm in the upper part of the galaxy (in Fig. 4.3 the black ellipse is on top of this arm). In NGC3368 this correlation between NUV break and reddening is less obvious, while the FUV break is more clear and present at the reddening point. Considering that this galaxy is particularly old according to the colour profile ($(FUV - NUV)_0 > 0.5$), this could be related to an scenario where the galaxy beyond the edge is populated by older migrated stars that still contribute to the NUV brightness of the galaxy. An extreme case where there is no correlation between the break and the reddening is the case of NGC4307. In this galaxy, the reddening is close to the centre, while a break in the NUV is observed at $\sim 85''$. While this break correlates with the visual boundary of the galaxy, the depth of the FUV data is not enough to detect this break in the FUV profile, and hence in the colour profile. Indeed, if we consider FUV as a tracer of star formation, with NUV more affected by older stars (see Hao et al. 2011), one interpretation of this profile could be that the recent star formation activity of this galaxy is concentrated in the inner $50''$, and beyond this point the NUV light is associated with older stellar populations. However, in both of the 4 cases mentioned here, the located edge (in NGC4307, the edge according to the NUV profile) is in good agreement with the apparent visual edge in the NUV images.

Finally, there are a few galaxies where, for various reasons, it is difficult to correlate a rim with an edge in the profiles. These are the cases of NGC3198, NGC4220, NGC4321, NGC5866 and NGC5907. The scenarios that cause this are different for each galaxy. In the case of NGC4220, for example, the surface

brightness and colour profiles indicate that the galaxy is particularly compact. This scenario is similar to the one presented by NGC4307, explained above, with the difference that in this case the surface brightness limit does not allow us to detect a break in the NUV profile where the edge appears on the image (around 110″). In addition, as noted in Sec. 2, this galaxy is morphologically classified as S0-a, so the stellar population is expected to be older in this type of galaxy.

More interesting are the cases of NGC3198 and NGC5907. In these cases we detect a first inner break in the colour profiles (and a truncation in the surface brightness profiles in NGC5907), but then we are able to detect a second further feature in the surface brightness profiles. In the case of NGC3198 this second edge is associated with a low surface brightness spiral arm at the top of the galaxy, which we will analyse in more detail in Sec. 5.2.2. In NGC5907, while the second feature is not observed in FUV because the image is not very deep, it is clearly visible in the NUV image. According to the NUV image (see Fig. 4.3), between the first truncation, determined here as R_{edge}, and the second feature there is an extension of the disk with lower brightness, ending in a warped shape caused by its interaction with dwarf galaxies (Shang et al. 1998; Martínez-Delgado et al. 2008). Since the truncations are linked to an in-situ star formation (Trujillo et al. 2020), the detection of a far away one could be linked to the ongoing star formation in the outermost region of the galaxy that has been triggered by a recent merger.

Finally, NGC4321 and NGC5866 do not show any obvious edges in their surface brightness profiles. The explanation for this abscence of edge comes from looking at the optical images. In Fig. 5.11 we show the colour images in optical wavelengths for both galaxies.

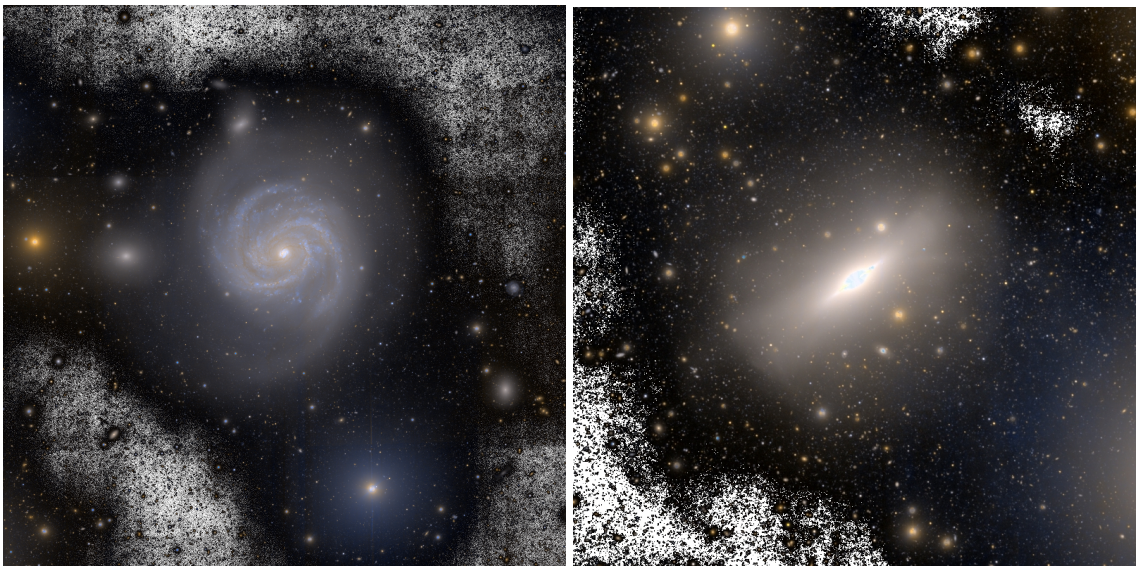

Figure 5.11: LIGHTS colour composed images of NGC4321 (21.5′ × 21.5′, left) and NGC5866 (15′ × 15′, right).

The optical colour give an indication of why a boundary is not well detected. In both cases, the galaxies are undergoing a merger. In the case of NGC4321, the uppermost dwarf galaxy (NGC4323) appears to be interacting with the galaxy, causing the stream observed in Fig. 5.11. This interaction wash out any potential edge of the galaxy. Moreover, a deficit of neutral hydrogen has already been observed (Cayatte et al. 1990), which would also correlate with a low star formation. In NGC5866, the scenario is even more extreme. The presence of different stellar streams at different positions, under the old stellar population and the star formation activity apparently reflected in the colour profiles, can be linked to a history of multiple mergers for this galaxy.

5.2.2. UV Low Surface Brightness features in the outermost regions of the galaxies

In this section, we highlight some of the low surface brightness features detected with the profiles obtained in this work.

Extended disk of NGC3198

One of the major scientific highlights of GALEX was the detection of extended UV disks (XUV-Disks) in nearby spiral galaxies. Gil de Paz et al. (2005) in NGC4625 or Thilker et al. (2005) in M83 presented the first results of star formation activity in the outskirts at larger distances than expected, i.e., well beyond the traditional extension in the optical given by the position of the isophote 26 mag arcsec^{-2} in the B-band. Thilker et al. (2007) extended this study up to 189 disk galaxies from the NGS survey, classifying them into two types of extended disks, and correlating these features with the imprints of galaxies growing in star formation activity at the outskirts. One of the galaxies detected with an XUV-Disk was NGC3198. In our profiles, as noted in the previous section, we are able to detect an extension of the disk up to $\sim 520''$ ($\sim$ 32.5 kpc). Looking at the NUV and FUV images, this extension seems to be associated with a low surface brightness ($\sim 30 - 31$ mag arcsec^{-2}) spiral arm in the northern part of the major axis.

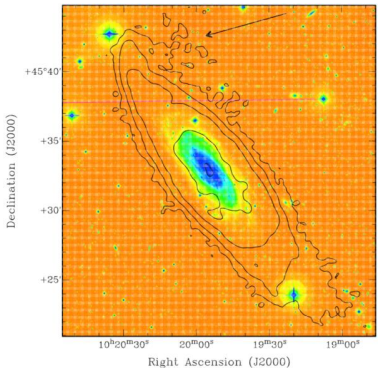

Figure 5.12: Fig. 2 of Gentile et al. (2013), showing the HI contours over the r-band image from HALOSTARS.

To better analyse this outter disk, we can compare our results with HI maps. Gentile et al. (2013) used data obtained with the Westerbork Synthesis Radio Telescope as part of the HALOGAS survey (Heald et al. 2011) to show the extension of HI in NGC3198. The results of this work suggest that the distribution of HI in NGC3198 is consistent with a prolongation of the stellar disk, with a radius slightly beyond the regions of star formation activity observed in Hα. Using deep r-band imaging of Isaac Newton Telescope (as part of HALOSTARS, Heald & HALOGAS Team 2012), they showed the extension of the HI disk when compared with deep, optical images (see Fig. 5.12).

In Fig. 5.13 we compare the HI map from Heald et al. (2011) with our FUV image and the LIGHTS LBT-g data. The HI map shows 3 spiral arms (green-yellow regions) apparently heading anti-clockwise. When the contour enclosing these arms is superimposed, the 1st and 2nd arms are clearly visible in the FUV image. These arms are enclosed by the black ellipse in Fig. 4.3. The 3rd arm is also visible in FUV as some clumps near the black outline. This 3rd arm is the cause of an extension in the profile up to the yellow ellipse in Fig. 4.3. For comparison, the 2nd and 3rd arms are less pronounced in the LIGHTS LBT-g band.

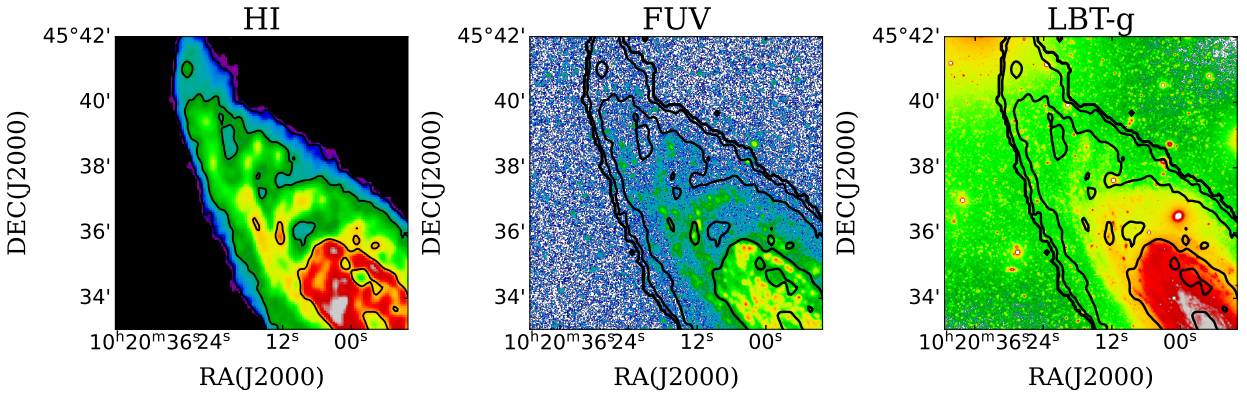

Figure 5.13: North-east part of NGC3198 in different bands: HI map from Gentile et al. (2013) (left), FUV band from this work, and LBT-g band from LIGHTS survey. Over plotted in black the 0, 0.1, 1, 5 and 15×10^{20} Jy beam^{-1} km s^{-1} contours of the HI map.

This outer spiral structure presented in the UV profiles may be related to a history of an inside-out growth of the disk (as noted for the XUV-Disks by Thilker et al. 2007). A more extended study should be done to establish how this growth is. Is it a smooth process or is it, on the contrary, a way fast event? A future developement of our work may shed light on the study of star formation activity at the edge of galaxies and its link with the evolution of galactic disks, taking as an example the detection of this structure in NGC3198.

Do we detect stellar haloes in NUV?

One of the main scientific goals of the LIGHTS survey, which we have used to select our sample, is to detect and characterise the stellar halo around galaxies. Therefore, one question we could explore is the possibility of detecting such faint components in our UV sample. Since *in-situ* star formation is not expected in stellar haloes (Cooper et al. 2010), we would expect the stellar haloes to be extremely faint in the UV, as these bands are a good proxy for the star formation activity. However, older stars could still contribute to the NUV and FUV emission of a galaxy (e.g., Hao et al. 2011, Sec. 5). Due to that, it would be reasonable to think that a sufficiently bright stellar halo could be visible in the UV, at fainter magnitudes than the optical bands.

However, this possible UV emission would be near or even beyond the limits of our dataset, as surface brightness in optical bands greater than 30 mag arcsec^{-2} is expected (Cooper et al. 2010). For example, in Trujillo et al. (2021) an asymmetric stellar halo was found for NGC1042, located at the northeastern part of the galaxy. This halo was observed in the surface brightness profiles between $\sim$ 220″ and $\sim$ 310″ with a surface brightness in g-band of $\sim$ 29 mag arcsec^{-2}. Looking at our profiles (Fig. 4.3), it is noticeable that our NUV profile of NGC1042 also reaches a flatter region beyond 220″ which does not follow an exponential profile. If this part is not tentatively related to the possible detection of the halo, the extremely low brightness ($\sim$ 31.5 mag arcsec^{-2}) suggest that it could also be due to reaching the limit of the image rather than observing a halo. Indeed, if we measure the profile where the stellar halo was not detected (see Trujillo et al. 2021, Fig. 3), this flat region is still observed (Fig. 5.14).

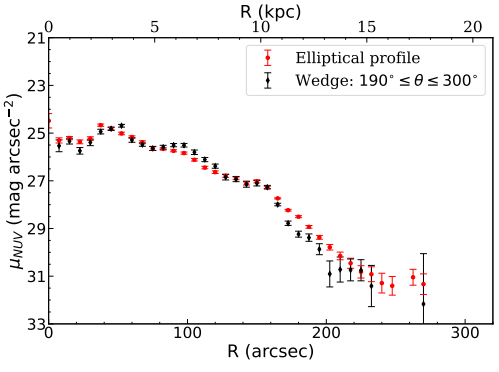

Figure 5.14: NUV profile of NGC1042: using the full ellipse (red) and using a wedge between 190° and 300° (black).

On the other hand, in NGC2712 we also observe a change in the exponential profile of a disk beyond $\sim 100''$. After carrying out tests to rule out the possibility of a bad masking, background subtraction or an underestimation of the PSF effect, it is possible to relate this excess of light to a real structure in the galaxy, since it is also bright enough ($\sim 29\,\mathrm{mag\,arcsec^{-2}}$) to discard effects of the data set limits. However, to relate this to a stellar halo, a more complete study using LBT optical data should be done, and here we only note the possibility of a relation between this excess of light and a stellar halo.

5.2.3. Preliminary studies of stellar population at the edge: NGC1042 and NGC3486

As mentioned in Sec. 1, one of the main reasons for making ultraviolet analysis of galaxies is to study their stellar populations, since young, OB stars are the main sources of the UV counterpart of galaxies. In this context, GALEX bands have been used to derive stellar population properties such as star formation rates (e.g., Kennicutt & Evans 2012) or ages. Bianchi (2011) showed that, in galaxies with a Cardelli et al. (1989) extinction law similar to that of the Milky Way, the dust correction in the colour profiles is small enough to consider $(FUV - NUV)$ colours as a good proxy for stellar ages, due to the location of the characteristic UV bump of dust extinction in the NUV band. In this section, we give a brief analysis of the stellar populations of NGC1042 and NGC3486. These galaxies are selected because they are M33-like, at similar distances, D$\sim$ 13 Mpc. In addition, they have similar low-inclination, making a comparison easier. We derive their stellar ages and SFRs.

For the stellar ages, we have used the $(FUV - NUV)$ colours of Bruzual & Charlot (2003) models of different ages and metallicities. We expect the stellar populations of these galaxies to be metal poorer than solar, and therefore we have used a sub-solar metallicity of $Z = 0.004$, corresponding to $[Fe/H] = -0.64$. Fig. 5.15 shows the results for NGC1042 and NGC3486 by colour-coding the $(FUV - NUV)$ profiles with stellar ages, bellow the age at the edge (the uncertainty is defined as the step in age from the models, as it is the dominant one).

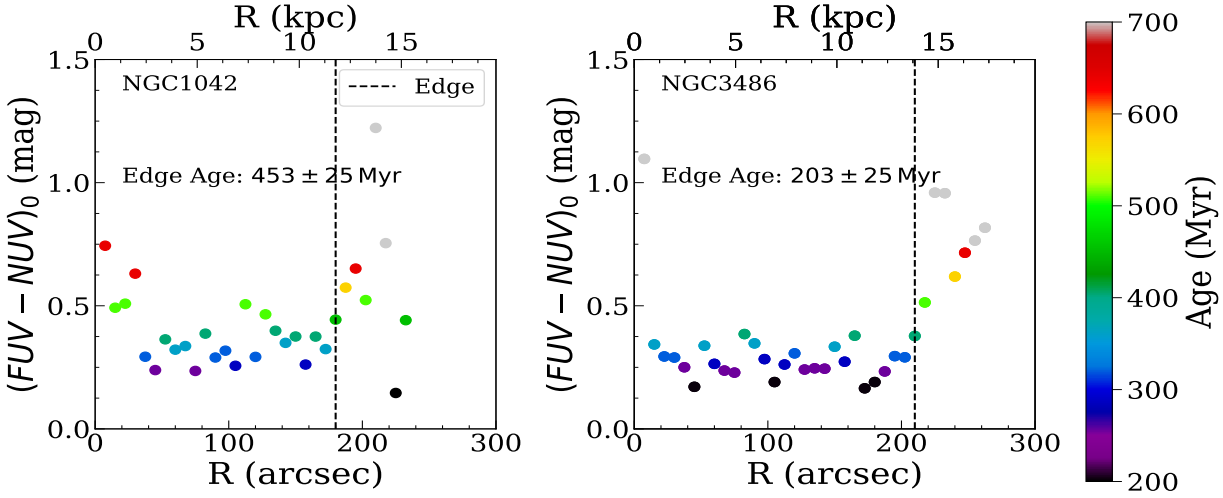

Figure 5.15: UV colour profiles of NGC1042 (left) and NGC3486 (right) colour-coded with the stellar ages at a fixed $[Fe/H] = -0.64$. A tentative age at the edge location (Tab. 4.1) is also given. $(FUV - NUV)$ uncertainties are not included for clarity.

According to the models, in NGC3486 an average age for the stellar population of the disk is ~ 200 Myr, similar along the entire disk. At the edge, the stellar population has an age of 203 ± 25 Myr. The behaviour of the stellar ages is similar for NGC1042 (colour profile is similar), but with ages of ~ 450 Myr (453 ± 25 Myr at the edge), about 2 times older. In both cases, the stars beyond the edge become older, consistent with a scenario where these stars could be originated inside the disk and migrated to outside, where there is

low or no star formation activity (Trujillo et al. 2020). Note that, without the PSF correction, the drop on the colour profiles (see Fig. 5.6) would lead to extremely young stellar populations according to the models.

The SFR can also be measured using ultraviolet data. Many papers have used FUV to derive a calibrator for SFR, since it has the advantage of being able to trace the star formation activity back to about 100 Myr (Kennicutt & Evans 2012). We have used the calibrations provided by two different works in order to derive SFR from FUV: Hao et al. (2011) and Brown et al. (2017). These works differ mainly in the method used to correct for FUV dust attenuation. Hao et al. (2011) calibrate the FUV correction by deriving empirical relations (using Moustakas & Kennicutt 2006 sample) with the infrared to FUV luminosity ratio (IRX) and with the FUV-NUV colour. They then calibrate the $SFR - L_{FUV}$ relation by computing it with STARBURST99 models using different IMFs. Here, we use dust attenuation calibration with FUV-NUV colours and SFRs for a Kroupa & Weidner (2003) IMF with constant star formation histories of 100 Myr and 1 Gyr (Eq. 5.1). On the other hand, Brown et al. (2017) explore two different dust corrections (see Sec. 5.1 of their work): with a Calzetti et al. (2000) extinction law (1) and with Hao et al. (2011) calibrations (2). They use the sample of Moustakas & Kennicutt (2006) to calibrate the ratio between FUV luminosity and $H\alpha$ luminosity, in order to measure the SFR with Kennicutt et al. (2009) calibration for a Kroupa IMF (Eq. 5.2). The equations involved are:

$$A_{\rm FUV} = 3.83[(FUV - NUV)_0 - 0.022]$$

$$SFR(\mathrm{M_\odot yr^{-1}}) = \mathrm{C_{FUV}} \times \mathrm{L_{FUV,corr}(erg/s)} \quad \begin{cases} \log C_{FUV}(100\,\mathrm{Myr}) = & -43.35 \\ \log C_{FUV}(1\,\mathrm{Gyr}) = & -43.384 \end{cases} \tag{5.1}$$

$$\left.\begin{aligned} \log L_{FUV} + 2(FUV - NUV)_0 = & \quad 42.42 + 0.96(\log L_{H\alpha,corr} - 40)\ (1) \\ \log L_{FUV} + 1.532(FUV - NUV)_0 - 0.0088 = & \quad 42.25 + 0.90(\log L_{H\alpha,corr} - 40)\ (2) \end{aligned}\right\} \tag{5.2}$$

$$SFR(\mathrm{M_\odot yr^{-1}}) = 5.5 \times 10^{-42} \mathrm{L_{H\alpha,corr}(erg\,s^{-1})}$$

We used both works to calculate the SFR in two different ways: measuring the local SFR (i.e., the SFR per unit area) at each distance from the centre, and integrating all SFR within a given radius (i.e., measuring the total SFR within a given ellipse). The results for NGC1042 are shown in Fig. 5.16 and for NGC3486 in Fig. 5.17. In both cases, the uncertainties are calculated by measuring the maximum and minimum values of the SFR due to error propagation of the coefficients (present in Hao et al. 2011; Brown et al. 2017) and uncertainties in the flux. For the dust extinction based on the colour, we used the mean $(FUV - NUV)$ colour in the disk, i.e., between $\sim 30''$ and the edge ($(FUV - NUV)_0 = 0.339$ in NGC1042 and $(FUV - NUV)_0 = 0.272$ in NGC3486).

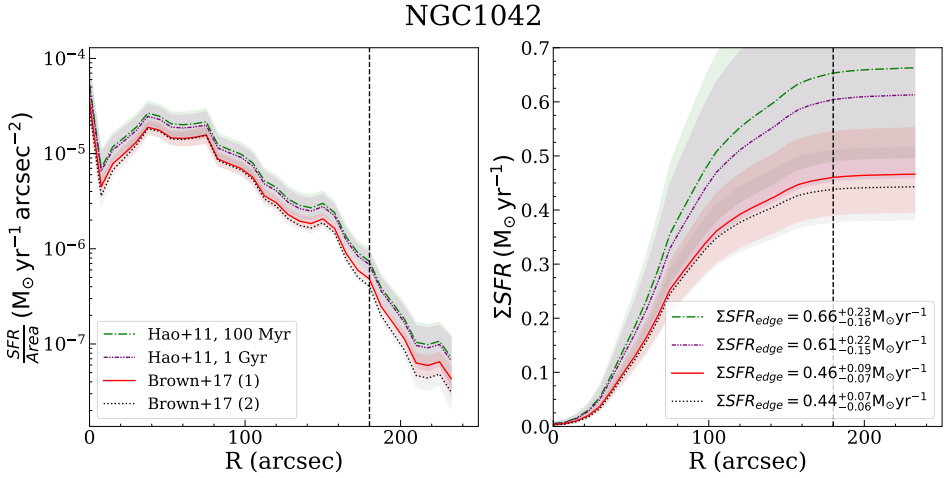

Figure 5.16: Surface SFR ($SFR/Area$) and cumulative SFR (ΣSFR) profiles of NGC1042 using different calibrations. Uncertainties are plotted as colored regions. The different equations used by Brown et al. (2017) for dust correction are refereed as *Brown+17 (1)* and *(2)* in the same order they appear in Eq. 5.2. Dashed black line represents the radial location of the edge, according to Tab. 4.1.

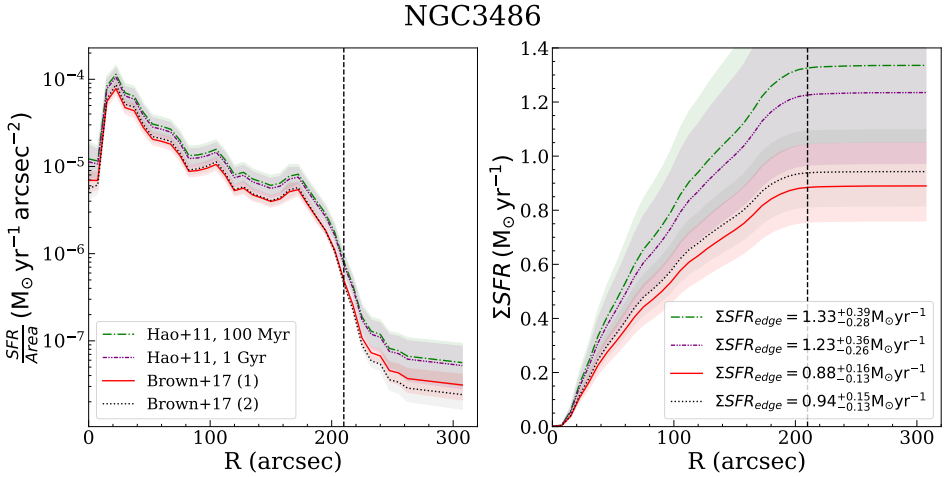

Figure 5.17: Same as Fig. 5.16 but for NGC3486.

Since SFRs are directly related to the FUV, the local SFR profiles have very similar shape as the FUV profiles, with a clear break around the edge of galaxies. Beyond this edge, the integrated SFRs reach an asymptotic value, again consistent with a scenario of no star formation after this point. This value is $0.2 - 0.3\,M_\odot yr^{-1}$ higher for Hao et al. (2011) calibrators in both galaxies. This difference is related to the assumptions in the models. Hao et al. (2011) calibrates the SFR for models with solar metallicities, which could lead to a higher SFR. On the other hand, Brown et al. (2017) find that their empirical calibrations of the $H\alpha$ luminosity mitigate the effect of the stellar population assumptions. With these calibrations, we obtain a global SFR for the whole galaxy extension (using the second dust attenuation correction) of $0.44^{+0.07}_{-0.06} M_\odot yr^{-1}$ in NGC1042; and $0.94^{+0.15}_{-0.12} M_\odot yr^{-1}$ in NGC3486. As with the stellar ages, the SFR in NGC3486 is 2 times larger than in NGC1042. However, a study including stellar masses (not available in this work) should be carried out in order to draw a proper conclusion from these results. Note again that if the PSF were not taken into account, there would be an excess of FUV at the end of the profiles, leading to an overestimation of the SFRs beyond the edge of these galaxies.

Although the SFR values are reasonable when compared with those galaxies of similar stellar mass (M33 has a SFR of $0.45\,M_\odot yr^{-1}$, Verley, S. et al. 2009), some considerations about their accuracy should be taken into account. First, as noted by Hao et al. (2011), dust attenuation calibrated with FUV-NUV colours has a larger scatter and its relationship is less linear than with IRX. They advise that it can be used when IR data are not available, but that it is not a good indicator of dust attenuation in normal star-forming galaxies. In addition, the range of applicability extends from $(FUV - NUV) = 0.07$ to $(FUV - NUV) = 1.06$, placing some of the galaxies in our sample outside this range. Since Brown et al. (2017) use similar dust attenuation calibrations, this also applies to the results with their calibrations. Second, the metallicities used in Hao et al. (2011) are solar, but this is mitigated by the use of Brown et al. (2017) calibrations. However, these calibrations are made for the total flux of galaxies, i.e., the integrated SFRs. Thus, the relations have only been explored from $L_{FUV} \gtrsim 10^{41} erg\,s^{-1}$, while for the measurement of local SFRs we use luminosities that are fainter, specially at the outermost regions. At those luminosities, the linearity of this relation has not yet been explored, and it should be used carefully. With these limitations, our SFR measurements, while reasonable, need a deeper analysis to test their reliability, and their applicability in the rest of the sample.

Chapter 6

Conclusions

The recent development of new observational and data reduction techniques in Astronomy has made it possible to observe the faintest regions of galaxies. This allows us to study their properties and their connection with galaxy evolution. In order to have a proper characterisation of these regions, a multi-wavelength analysis should be performed. In this work, we present the study of a sub-sample of 16 galaxies from the optical ultra-deep LIGHTS survey in the ultraviolet (in addition to IC3211 in the field of NGC4307). We use GALEX data in the far and near UV, in a low surface brightness context. In this study, we develop a new methodology for the analysis of GALEX data, based on the techniques used in the optical counterparts and on previous UV works. The methodology can be summarised in two steps:

- We characterise the background as a single mean value around the galaxy, following procedures similar to those used in other UV studies (e.g., Gil de Paz et al. 2007). To remove the background, we build a Poissonian statistical background with this mean value. The removal of a Poissonian random distribution generates a Gaussian-like distribution. We show that this strategy allows us to use low surface brightness optimised detection software, such as NoiseChisel, which assumes a Gaussian-like nature of the background.

- We apply the deconvolution algorithms developed by Golini et al. (in prep.) to characterise and subtract the effects of PSF convolution in the faint end of the UV profiles. In this context, we present a new characterisation for GALEX PSFs, extended up to 750″ versus the 90″ available in the GALEX archives. To characterise our galaxies in the UV, we combine a single/broken exponential model with the real data in the inner part.

We present the results of applying both steps in the form of surface brightness and colour (where FUV is available) profiles. We show that this methodology yields surface brightness depths of $\sim 28.5 - 30.5\,\mathrm{mag\,arcsec^{-2}}$ (3σ, $10'' \times 10''$), with radial profiles reaching reliable magnitudes as faint as $\sim 31\,\mathrm{mag\,arcsec^{-2}}$, about 1 magnitude deeper than in previous GALEX studies. We also compare these results with the GALEX pipeline data, showing that:

a) Our background subtraction strategy is able to avoid structures that cause over-subtraction in the GALEX pipeline in some galaxies, such as NGC3198 or NGC3368. We theorise that these structures may be caused by poor source detection when characterising the background.

b) Our set of PSFs is able to explain the apparent excess of light in some FUV profiles, particularly in the extreme cases of NGC1042, NGC2903 and NGC3486. We demonstrate that the subtraction of this PSF is crucial to obtain accurate FUV profiles in the outskirts.

This comparison highlights the significance of employing a rigorous analysis methodology. An over-subtraction of the background could result in the dilution of the faintest structures of galaxies on the surface brightness profiles, as observed in the case of NGC3198. In contrast, the impact of the FUV PSF is found to be the most significant discrepancy when compared to the GALEX pipeline. If not accounted for, we demonstrate that this effect results in $(FUV - NUV)_0$ colour profiles becoming bluer due to a brighter FUV profile. If the PSF effect is not corrected, one would assume there are extremely young

stellar populations and higher levels of star formation activity in regions where we see no evidence this is happening, i.e., there are no star-forming clumps, etc.

Our methodology is employed to analyse in a qualitative way the profiles of the galaxies. In 76% of the sample, a well defined edge can be found using surface brightness and colour profiles, although it should be noted that the resolution of the GALEX bands should be taken into account when determining the accuracy of these measurements. In the majority of cases, the edge is in agreement with the visual optical border of the galaxy. It is noteworthy that the surface brightness depths reached by NUV permit the detection of edges in NGC4307 and NGC5907 at grater distances than those anticipated from colour profiles, yet in accordance with the images. Furthermore, a more detailed analysis of the edge of NGC3198 is presented, demonstrating that an extension is observed in agreement with the one observed by HI maps. Additionally, the observed excess of light in select NUV profiles, including that of NGC2712, may be indicative of presence of stellar haloes. However, a more comprehensive analysis, utilising optical data, is warranted, given the faint nature of such structures.

Finally, we demonstrate the potential of our data in the analysis of stellar populations at the edge of galaxies. A preliminary study of the stellar populations of NGC1042 and NGC3486 is presented here, utilising the models of Bruzual & Charlot (2003) for stellar ages and different established calibrators of star formation rates. The measurements of stellar ages and star formation rates at the detected edges of these galaxies are presented. However, it should be noted that the accuracy of the calibrators should be considered when analysing the results.

In conclusion, this study presents the ultraviolet counterpart of the LIGHTS survey, with the objective of understanding how the galaxies grow with time and how their edges move from inside-out. Moreover, the methodology developed here yields some of the deepest results in ultraviolet studies of galaxies to date, and could prove beneficial in future ultraviolet analysis, not only with GALEX, but also with more recent UV telescopes such as UVIT/AstroSat (Tandon et al. 2017).

Bibliography

Abramowitz, M. & Stegun, I. A. 1948, Handbook of mathematical functions with formulas, graphs, and mathematical tables, Vol. 55 (US Government printing office)

Ahn, C. P., Alexandroff, R., Allende Prieto, C., et al. 2012, The Astrophysical Journal Supplement Series, 203, 21

Aihara, H., Armstrong, R., Bickerton, S., et al. 2018, Publications of the Astronomical Society of Japan, 70, S8

Akhlaghi, M. 2019a, arXiv e-prints, arXiv:1909.11230

Akhlaghi, M. 2019b, Astronomical Society of the Pacific Conference Series, 521, 299

Akhlaghi, M. & Ichikawa, T. 2015, The Astrophysical Journal Supplement Series, 220, 1

Azzollini, R., Trujillo, I., & Beckman, J. E. 2008, The Astrophysical Journal, 679, L69

Bakos, J., Trujillo, I., & Pohlen, M. 2008, The Astrophysical Journal, 683, L103

Bertin, E. & Arnouts, S. 1996, Astronomy and Astrophysics Supplement Series, 117, 393

Bianchi, L. 2011, Astrophysics and Space Science, 335, 51

Bianchi, L. 2014, Astrophysics and Space Science, 354, 103

Bianchi, L., Conti, A., & Shiao, B. 2014, Advances in Space Research, 53, 900

Bianchi, L., Shiao, B., & Thilker, D. 2017, The Astrophysical Journal Supplement Series, 230, 24

Boissier, S., Gil de Paz, A., Boselli, A., et al. 2008, The Astrophysical Journal, 681, 244

Bouquin, A. Y. K., Gil de Paz, A., Muñoz-Mateos, J. C., et al. 2018, The Astrophysical Journal Supplement Series, 234, 18

Brown, M. J. I., Moustakas, J., Kennicutt, R. C., et al. 2017, The Astrophysical Journal, 847, 136

Bruzual, G. & Charlot, S. 2003, Monthly Notices of the Royal Astronomical Society, 344, 1000

Buitrago, F. & Trujillo, I. 2024, Astronomy and Astrophysics, 682, A110

Bullock, J. S. & Johnston, K. V. 2005, The Astrophysical Journal, 635, 931

Calzetti, D., Armus, L., Bohlin, R. C., et al. 2000, The Astrophysical Journal, 533, 682

Cardelli, J. A., Clayton, G. C., & Mathis, J. S. 1989, The Astrophysical Journal, 345, 245

Cayatte, V., van Gorkom, J. H., Balkowski, C., & Kotanyi, C. 1990, The Astronomical Journal, 100, 604

Chamba, N., Trujillo, I., & Knapen, J. H. 2022, Astronomy and Astrophysics, 667, A87

Cooper, A. P., Cole, S., Frenk, C. S., et al. 2010, Monthly Notices of the Royal Astronomical Society, 406, 744

De Jong, R. S. 2008, Monthly Notices of the Royal Astronomical Society, 388, 1521

Gentile, G., Józsa, G. I. G., Serra, P., et al. 2013, Astronomy and Astrophysics, 554, A125

Gil de Paz, A., Boissier, S., Madore, B. F., et al. 2007, The Astrophysical Journal Supplement Series, 173, 185

Gil de Paz, A., Madore, B. F., Boissier, S., Swaters, R., et al. 2005, The Astrophysical Journal, 627, L29

Hao, C.-N., Kennicutt, R. C., Johnson, B. D., et al. 2011, The Astrophysical Journal, 741, 124

Heald, G., Józsa, G., Serra, P., et al. 2011, Astronomy and Astrophysics, 526, A118

Heald, G. H. & HALOGAS Team. 2012, in American Astronomical Society Meeting Abstracts, Vol. 219, American Astronomical Society Meeting Abstracts #219, 346.24

Hunt, B. 1971, IEEE Transactions on Audio and Electroacoustics, 19, 285

Infante-Sainz, R. & Akhlaghi, M. 2024, Research Notes of the American Astronomical Society, 8, 10

Infante-Sainz, R., Akhlaghi, M., & Eskandarlou, S. 2024, Research Notes of the American Astronomical Society, 8, 22

Infante-Sainz, R., Trujillo, I., & Román, J. 2020, Monthly Notices of the Royal Astronomical Society, 491, 5317

Ivezić, Ž., Kahn, S. M., Tyson, J. A., et al. 2019, The Astrophysical Journal, 873, 111

Jablonka, P., Tafelmeyer, M., Courbin, F., & Ferguson, A. M. N. 2010, Astronomy and Astrophysics, 513, A78

Kelvin, L. S., Hasan, I., & Tyson, J. A. 2023, Monthly Notices of the Royal Astronomical Society, 520, 2484

Kennicutt, Robert C., J., Hao, C.-N., Calzetti, D., et al. 2009, The Astrophysical Journal, 703, 1672

Kennicutt, R. C. & Evans, N. J. 2012, Annual Review of Astronomy and Astrophysics, 50, 531

Kroupa, P. & Weidner, C. 2003, The Astrophysical Journal, 598, 1076

Martin, D. C., Fanson, J., Schiminovich, D., et al. 2005, The Astrophysical Journal, 619, L1

Martínez-Delgado, D., Cooper, A. P., Román, J., et al. 2023, Astronomy and Astrophysics, 671, A141

Martínez-Delgado, D., Peñarrubia, J., Gabany, R. J., et al. 2008, The Astrophysical Journal, 689, 184

Martínez-Lombilla, C., Trujillo, I., & Knapen, J. H. 2019, Monthly Notices of the Royal Astronomical Society, 483, 664

Morrissey, P., Conrow, T., Barlow, T. A., et al. 2007, The Astrophysical Journal Supplement Series, 173, 682

Moustakas, J. & Kennicutt, Robert C., J. 2006, The Astrophysical Journal Supplement Series, 164, 81

Oke, J. B. & Gunn, J. E. 1983, The Astrophysical Journal, 266, 713

Román, J., Rich, R. M., Ahvazi, N., et al. 2023, Astronomy and Astrophysics, 679, A157

Roškar, R., Debattista, V. P., Stinson, G. S., et al. 2008, The Astrophysical Journal, 675, L65

Sandin, C. 2014, Astronomy and Astrophysics, 567, A97

Shang, Z., Zheng, Z., Brinks, E., et al. 1998, The Astrophysical Journal, 504, L23

Skellam, J. G. 1946, Journal of the Royal Statistical Society, 109, 296

Tandon, S. N., Subramaniam, A., Girish, V., et al. 2017, The Astronomical Journal, 154, 128

Thilker, D. A., Bianchi, L., Boissier, S., et al. 2005, The Astrophysical Journal, 619, L79

Thilker, D. A., Bianchi, L., Meurer, G., et al. 2007, The Astrophysical Journal Supplement Series, 173, 538

Trujillo, I., Chamba, N., & Knapen, J. H. 2020, Monthly Notices of the Royal Astronomical Society, 493, 87

Trujillo, I., D'Onofrio, M., Zaritsky, D., et al. 2021, Astronomy and Astrophysics, 654, A40

Trujillo, I. & Fliri, J. 2016, The Astrophysical Journal, 823, 123

Verley, S., Corbelli, E., Giovanardi, C., & Hunt, L. K. 2009, Astronomy and Astrophysics, 493, 453

Watkins, A. E., Kaviraj, S., Collins, C. C., et al. 2024, Monthly Notices of the Royal Astronomical Society, 528, 4289

Wiener, N. 1949, Extrapolation, interpolation, and smoothing of stationary time series: with engineering applications (The MIT press)

Zaritsky, D., Golini, G., Donnerstein, R., Trujillo, I., et al. 2024, arXiv e-prints, arXiv:2406.01912

Appendix A

Full comparison with Galex Pipeline

The following graphs present a comprehensive comparison between our methodology and the GALEX pipeline, with the exception of NGC3486 (present in Sec. 5.1.2). In these figures, *UV LSB* refers to profiles obtained from images using our background subtraction criteria, while *PSF deconvolved* represents final profiles after applying the PSF deconvolution algorithms described in Sec. 3.2. *GALPIP* are the profiles obtained from GALEX pipeline background subtracted intensity maps (see Morrissey et al. 2007).

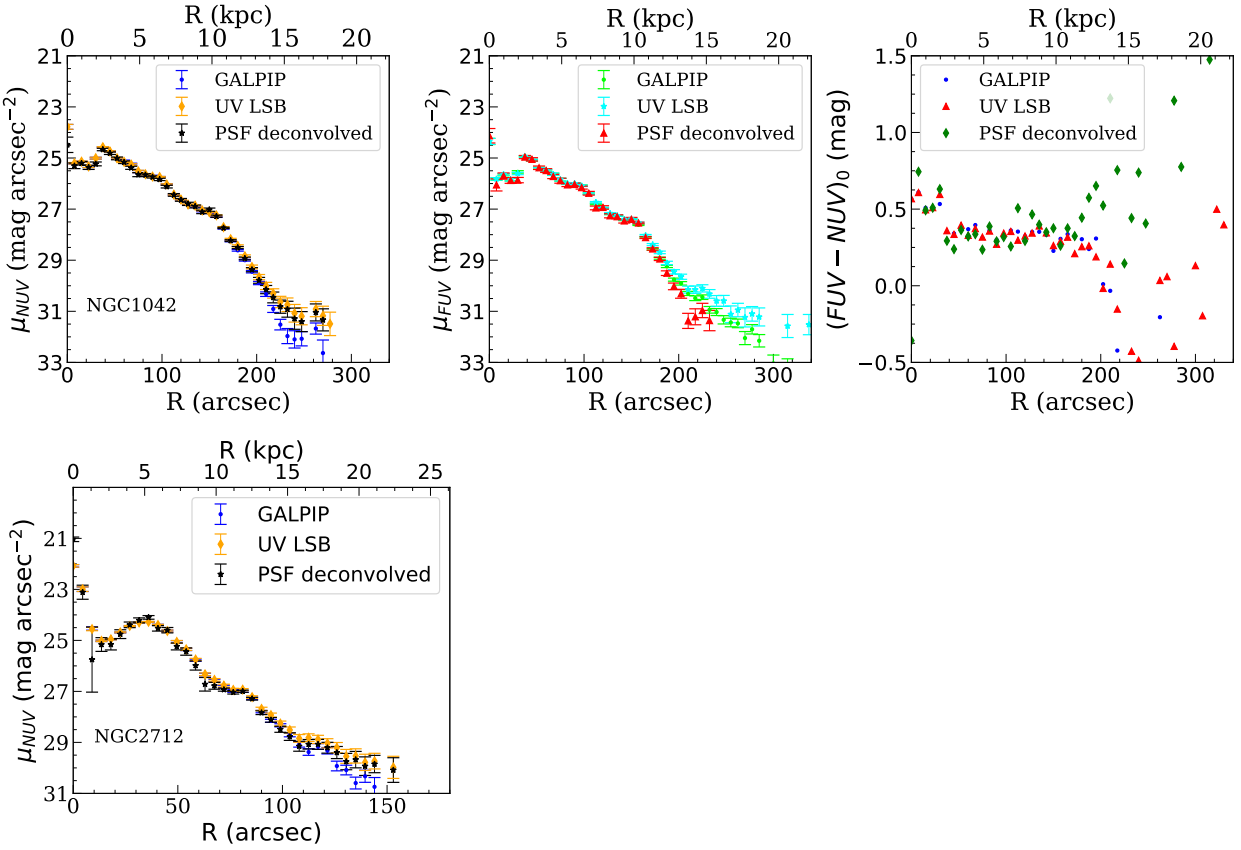

Figure A.1: Comparisson between our methodology and GALEX pipeline results. Left panel represents NUV profiles, middle pannel represents FUV profiles (if available) and right pannel shows colour profiles (without uncertainties for clearance).

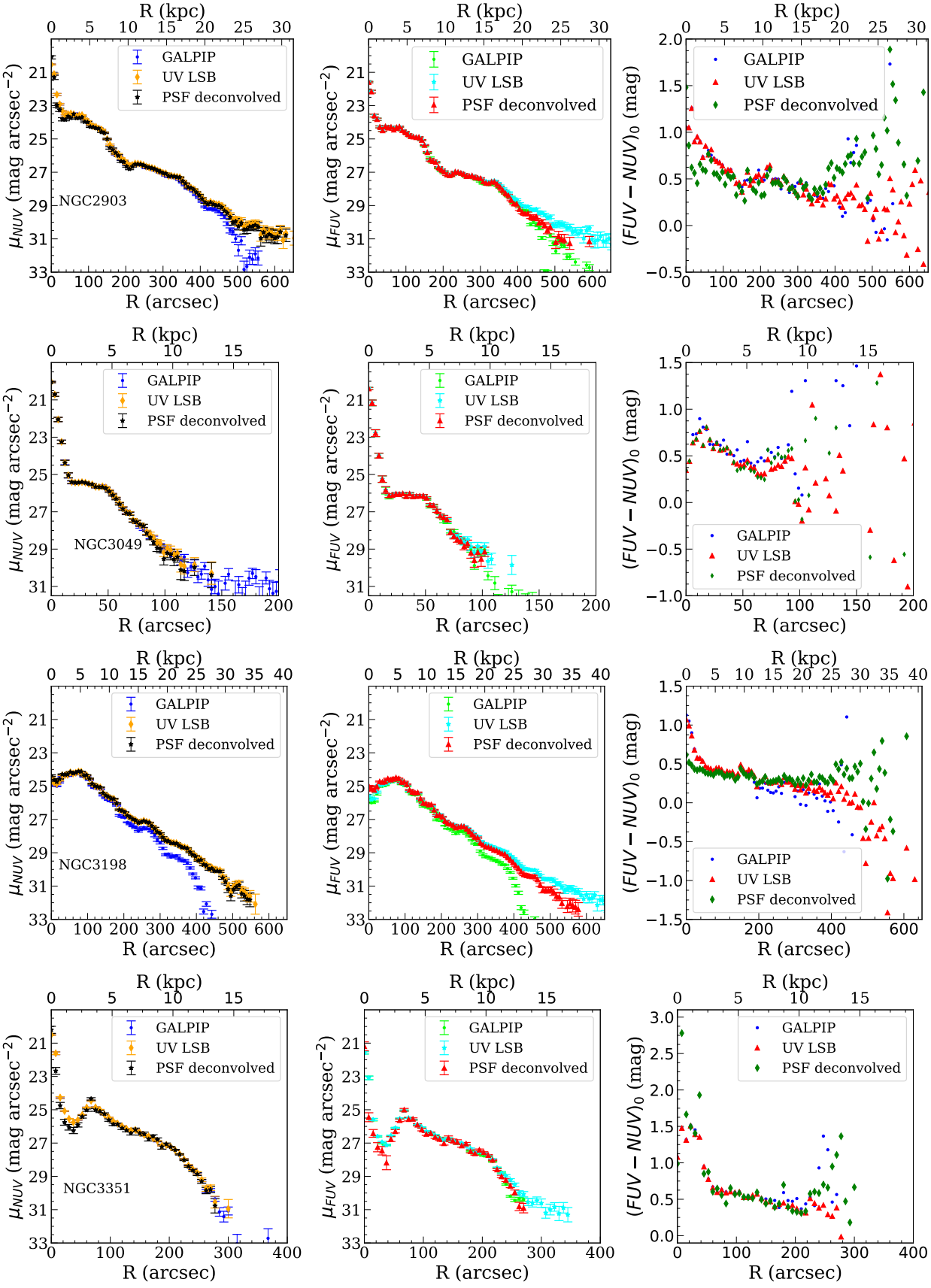

Figure A.1: Cont.

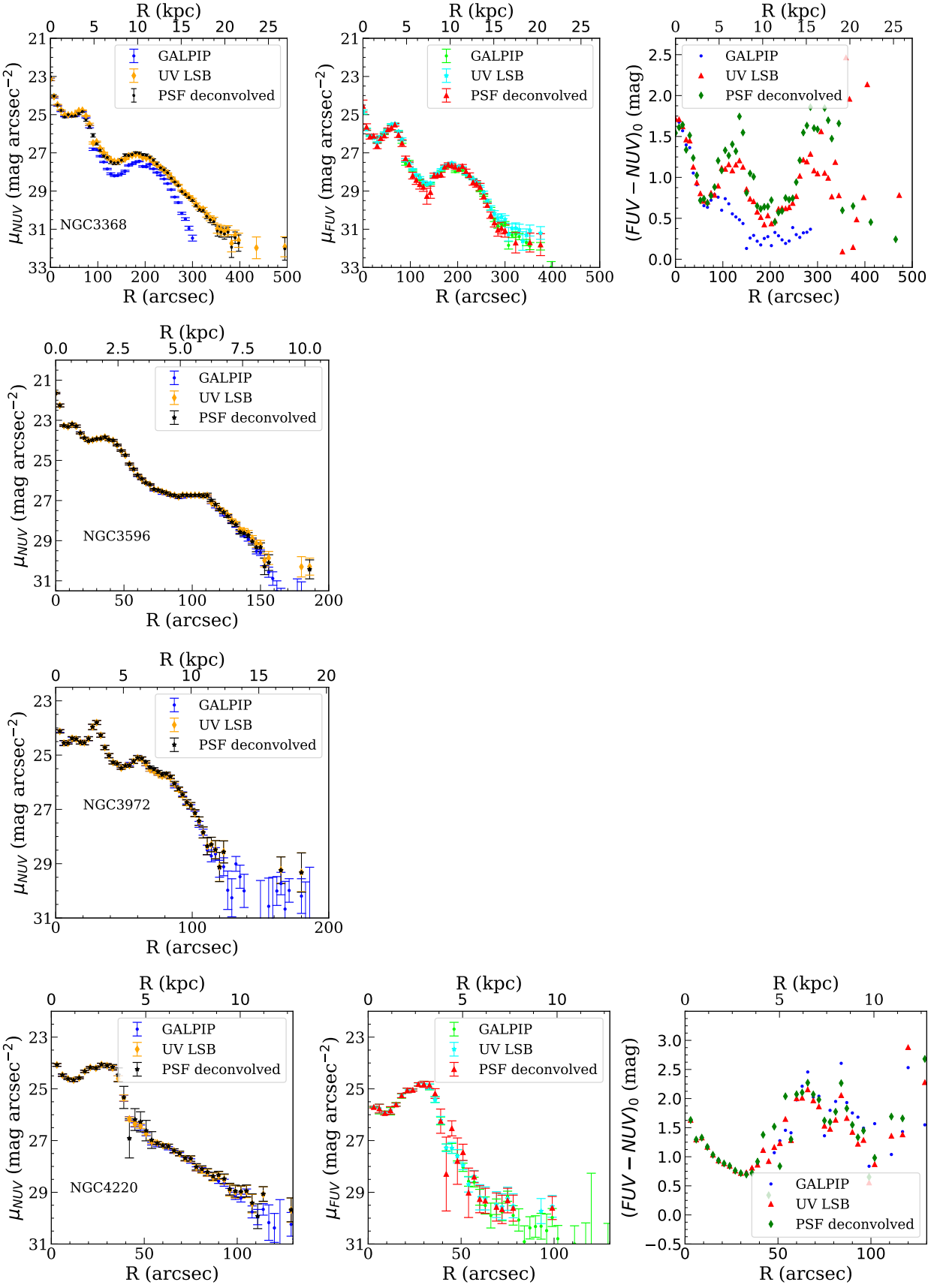

Figure A.1: Cont.

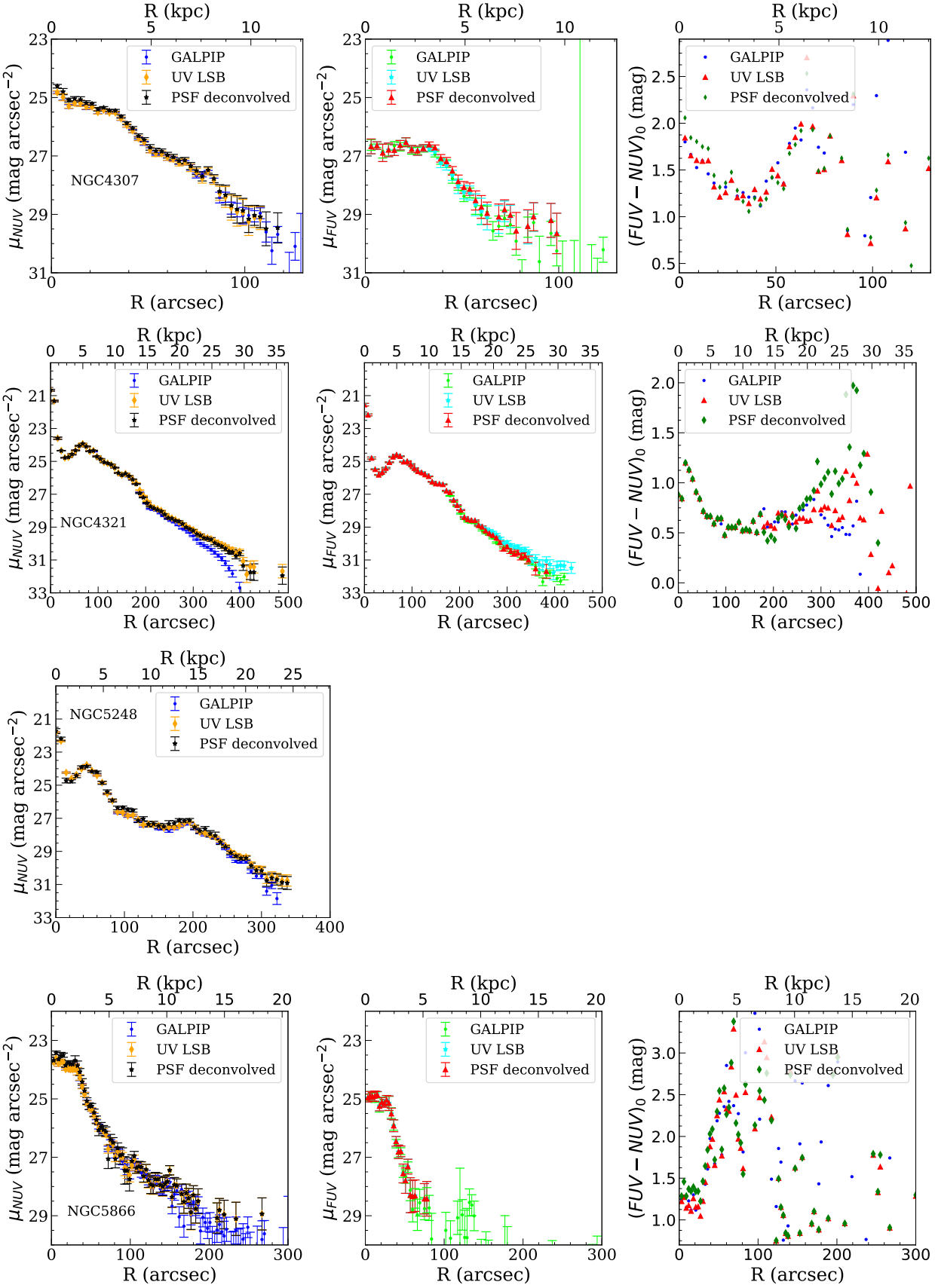

Figure A.1: Cont.

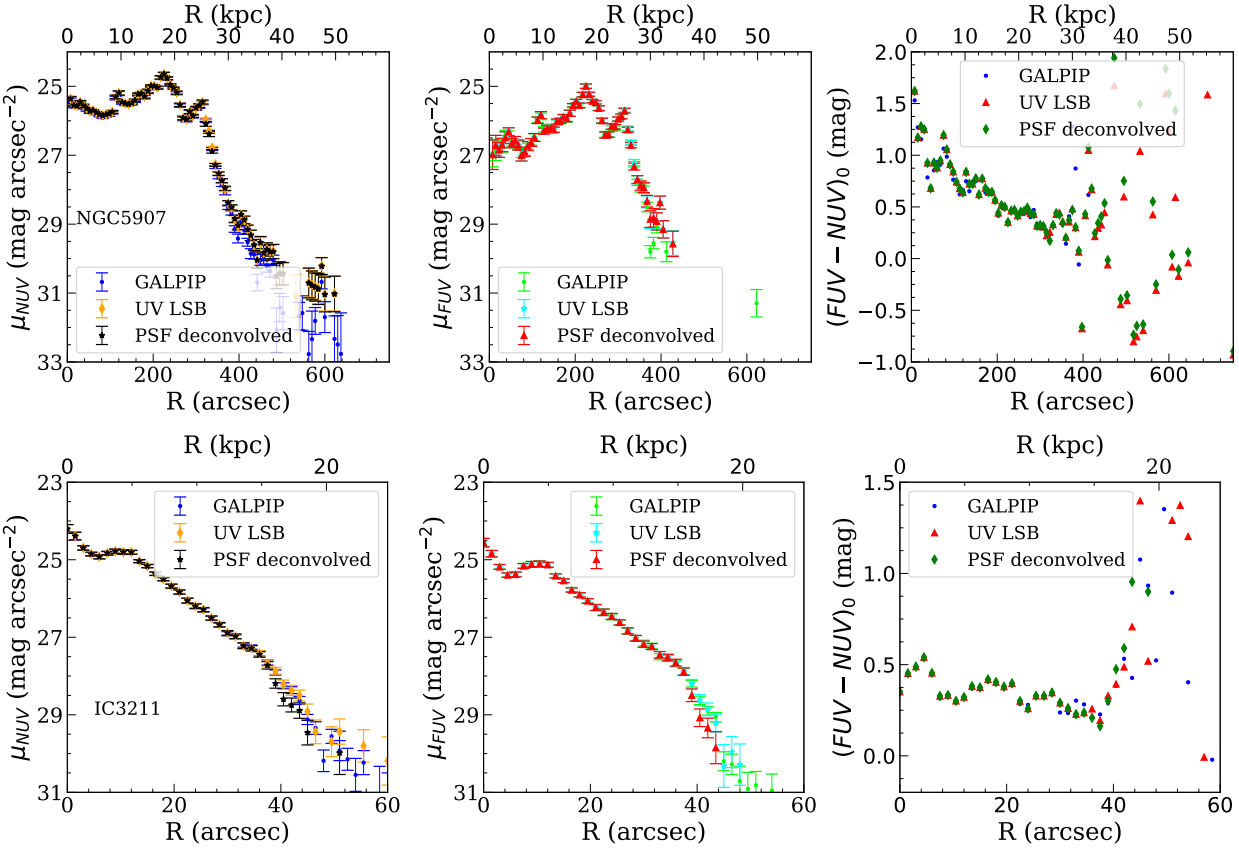

Figure A.1: Cont.

Appendix B

Subtraction of two Poisson distributions

In this work, we use the subtraction of two Poisson distributions with the same mean to demonstrate that the resulting distribution is similar to a Gaussian centred on 0. However, it should be noted that the theoretical distribution is not exactly Gaussian. In a previous study, Skellam (1946) demonstrated that the probability distribution of the difference between two Poisson distributions, $P(K = X - Y)$, can be expressed as a function of the probability distribution of the individual variables, $P(X = \mu_1)$, $P(Y = \mu_2)$, as

$$p(k; \mu_1, \mu_2) = Pr\{K = k\} = e^{-(\mu_1+\mu_2)} \left(\frac{\mu_1}{\mu_2}\right)^{k/2} I_k(2\sqrt{\mu_1\mu_2}) \tag{B.1}$$

where $I_k(x)$ is the modified Bessel function of the first kind. Then, Abramowitz & Stegun (1948) demonstrated that, in the case where $\mu_1 = \mu_2$ (such as in this work), the Skellam distribution can be approximated by an asymptotic expansion of the Bessel function:

$$p(k; \mu, \mu) \sim \frac{1}{\sqrt{4\pi\mu}} \left[1 + \sum_{n=1}^{\infty} (-1)^n \frac{\{4k^2 - 1\}\{4k^2 - 3^2\} \cdots \{4k^2 - (2n-1)^2\}}{n! 2^{3n} (2\mu)^n}\right] \tag{B.2}$$

Eq. B.2, for sufficiently large values of k, can be approach to a normal distribution of $\sigma = \sqrt{2\mu}$:

$$p(k; \mu, \mu) \sim \frac{e^{-k^2/4\mu}}{\sqrt{4\pi\mu}} \tag{B.3}$$

Fig. B.1 illustrates the Skellam distribution for typical backgrounds of our data. These are characterised by a mean of $\mu = 0.5$ for typical FUV, $\mu = 5$ for low NUV backgrounds, and $\mu = 15$ for high NUV backgrounds. Overlaid on this are the approximations to a normal distribution, as described by eq. B.3. The graphs indicate that it is reasonable to posit that, when subtracting the background as a Poisson distribution, the resulting distribution is similar to a normal distribution, with greater similarity observed when the background is higher. Therefore, these mathematical properties of the Poissonian distributions we use in this work is key to allow software such as NoiseChisel to be applied in our data set. This is because this type of software assumes a Gaussian statistics for the background to identify the sources of the images.

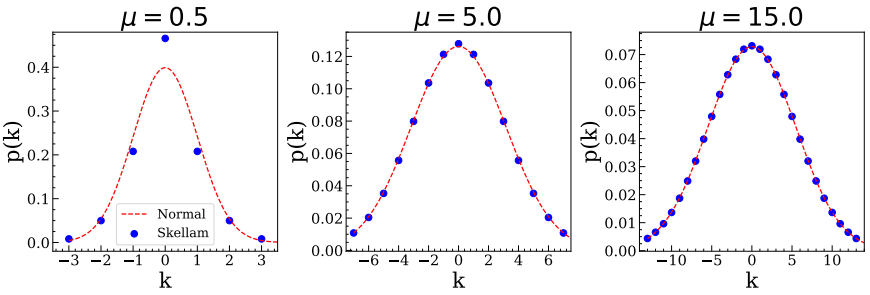

Figure B.1: Skellam distribution for $\mu_1 = \mu_2 = \mu$ compared with Normal distribution centered on 0 with $\sigma = \sqrt{2\mu}$.